2021

STUDY OF STRESS-BASED FIBER REORIENTATION LAW IN A FINITE ELEMENT MODEL OF CARDIAC TISSUE

Alexus Lori Rockward
University of Kentucky, alexus.rockward@gmail.com
Author ORCID Identifier:
https://orcid.org/0000-0003-0057-1877
Digital Object Identifier: https://doi.org/10.13023/etd.2021.348

STUDENT AGREEMENT:

I represent that my thesis or dissertation and abstract are my original work. Proper attribution has been given to all outside sources. I understand that I am solely responsible for obtaining any needed copyright permissions. I have obtained needed written permission statement(s) from the owner(s) of each third-party copyrighted matter to be included in my work, allowing electronic distribution (if such use is not permitted by the fair use doctrine) which will be submitted to UKnowledge as Additional File.

I hereby grant to The University of Kentucky and its agents the irrevocable, non-exclusive, and royalty-free license to archive and make accessible my work in whole or in part in all forms of media, now or hereafter known. I agree that the document mentioned above may be made available immediately for worldwide access unless an embargo applies.

I retain all other ownership rights to the copyright of my work. I also retain the right to use in future works (such as articles or books) all or part of my work. I understand that I am free to register the copyright to my work.

REVIEW, APPROVAL AND ACCEPTANCE

The document mentioned above has been reviewed and accepted by the student's advisor, on behalf of the advisory committee, and by the Director of Graduate Studies (DGS), on behalf of the program; we verify that this is the final, approved version of the student's thesis including all changes required by the advisory committee. The undersigned agree to abide by the statements above.

Alexus Lori Rockward, Student

Dr. Jonathan F. Wenk, Major Professor

Dr. Alexandre Martin, Director of Graduate Studies

STUDY OF STRESS-BASED FIBER REORIENTATION LAW IN A FINITE ELEMENT MODEL OF CARDIAC TISSUE

THESIS

A thesis submitted in partial fulfillment of the
requirements for the degree of Master of Science in Mechanical Engineering in the
College of Engineering
at the University of Kentucky

By

Alexus Lori Rockward

Lexington, Kentucky

Co- Directors: Dr. Jonathan F. Wenk, Professor of Mechanical Engineering

and Dr. Kenneth S. Campbell, Professor of Physiology

Lexington, Kentucky

2021

https://orcid.org/0000-0003-0057-1877

ABSTRACT OF THESIS

STUDY OF STRESS-BASED FIBER REORIENTATION LAW IN A FINITE ELEMENT MODEL OF CARDIAC TISSUE

Myofiber organization in the heart plays an important role in achieving and maintaining physiological cardiac function. In many cardiac disease states, myofibers and particularly cardiomyocytes are disorganized in chaotic patterns, a phenotype known broadly as myocardial disarray. In familial hypertrophic cardiomyopathy (HCM), this disorganization in the form of myocyte disarray is thought to contribute to impaired cardiac function and the development of arrhythmia during disease progression. However, the mechanisms regarding fiber reorientation in the heart are yet still unclear, and few adaptative laws have been created to explore these mechanisms. A stretch-based law was developed with the aim of achieving physiological fiber organization from a non-physiological starting point, but it was not sufficient to reproduce the normal human architecture. Adaptation under pathological conditions was not attempted.

We hypothesize that reorientation occurs in cardiac tissue such that shear stresses are minimized and that this mechanism, in tandem with local mechanical heterogeneities caused by certain disease states, is responsible for the development of disarray. The aim of this work was to propose a novel stress-based fiber reorientation law and assess its potential to induce myocardial disarray in a computational model of the heart. The law was implemented in a finite element framework with simple mesh geometries and tested against known mechanics solutions. Then, heterogeneities in passive and contractile properties among mesh elements was introduced, and the fiber orientations adapted under cyclical loading conditions were evaluated. Stress-based reorientation produced well-organized orientations for homogeneous structures and fiber disorganization for structures with heterogeneous passive or contractile properties. We conclude that the stress-based reorientation law proposed in this work can potentially characterize fiber adaptation in the heart and could be used to develop myocardial disarray in a cardiac model. Further work includes the implementation of the reorientation law in a left ventricle model and the validation of results with experimental studies.

KEYWORDS: Fiber Remodeling, Myocyte Disarray, Cardiac Remodeling, Fiber Adaptation

Alexus Lori Rockward

(Name of Student)

07/16/2021

Date

STUDY OF STRESS-BASED FIBER REORIENTATION LAW IN A FINITE ELEMENT MODEL OF CARDIAC TISSUE

By
Alexus Lori Rockward

Jonathan F. Wenk
Co-Director of Dissertation

Kenneth S. Campbell
Co-Director of Dissertation

Alexandre Martin
Director of Graduate Studies

07/16/2021
Date

ACKNOWLEDGMENTS

First, thanks be to the Godhead without whom this thesis would truly not come into existence. Additionally, this work would not be possible with the help of several people. Special thanks to Dr. Jonathan Wenk whose insights and constant guidance throughout the course of this project helped give shape to this work. His academic instruction in continuum mechanics as well as his example of rigorous yet flexible thinking as a principal investigator will serve as a guide throughout my research career. A special thanks to Charles Mann as well for his unwavering patience and technical support as I learned the finite element framework on which my project depends. Thank you to Dr. Kenneth Campbell for his mentorship and providing invaluable insights concerning cardiac physiology and to Dr. Lik-Chaun Lee and Joy Mojumder for serving as challenging and refining influences on this project. Finally, thanks to my friends and family for the emotional support that sustained me throughout the challenging phases of this project.

.

TABLE OF CONTENTS

LIST OF TABLES

LIST OF FIGURES

CHAPTER 1. INTRODUCTION

1.1 Myocardial Disarray

The human heart has a complex 3D fiber-reinforced structure. The fiber orientation varies continuously from +60º at the endocardium and -60º at the epicardium, producing a left-handed spiral from the subendocardium to midwall and a right-handed spiral from midwall to subepicardium, as shown in Figure 1.1 (Rohmer et al., 2007). The myofibers are further organized into laminar sheets approximately four myofibers thick. The myofibers are arranged largely parallel to one another and bound together between cleavage planes by a network of collagen fibers and extracellular matrix (ECM). The sheets formed by the cleavage planes are connected to their neighbors via another network of collagen called the perimysium. The details of this architecture are shown in Figure 1.2. This complex fiber architecture contributes to proper cardiac function by enabling the torsion required to maximize blood ejection. The orthotropic passive properties of cardiac tissue also stem from the fiber families associated with myofiber orientation as well as the collagen networks.

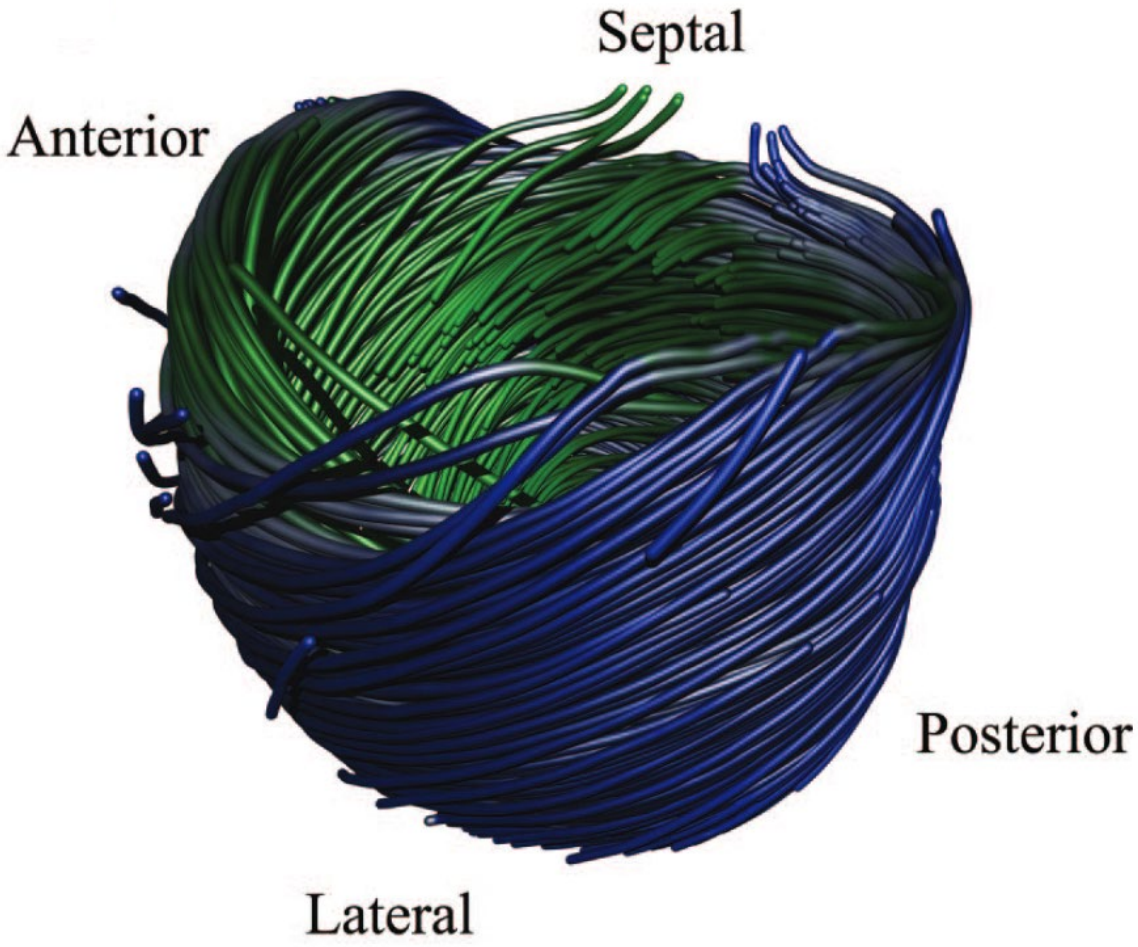

Figure 1.1 Visualization of normal fiber architecture in human left ventricle reconstructed from DTMRI. Adapted with permission from Rohmer et al. (2007).

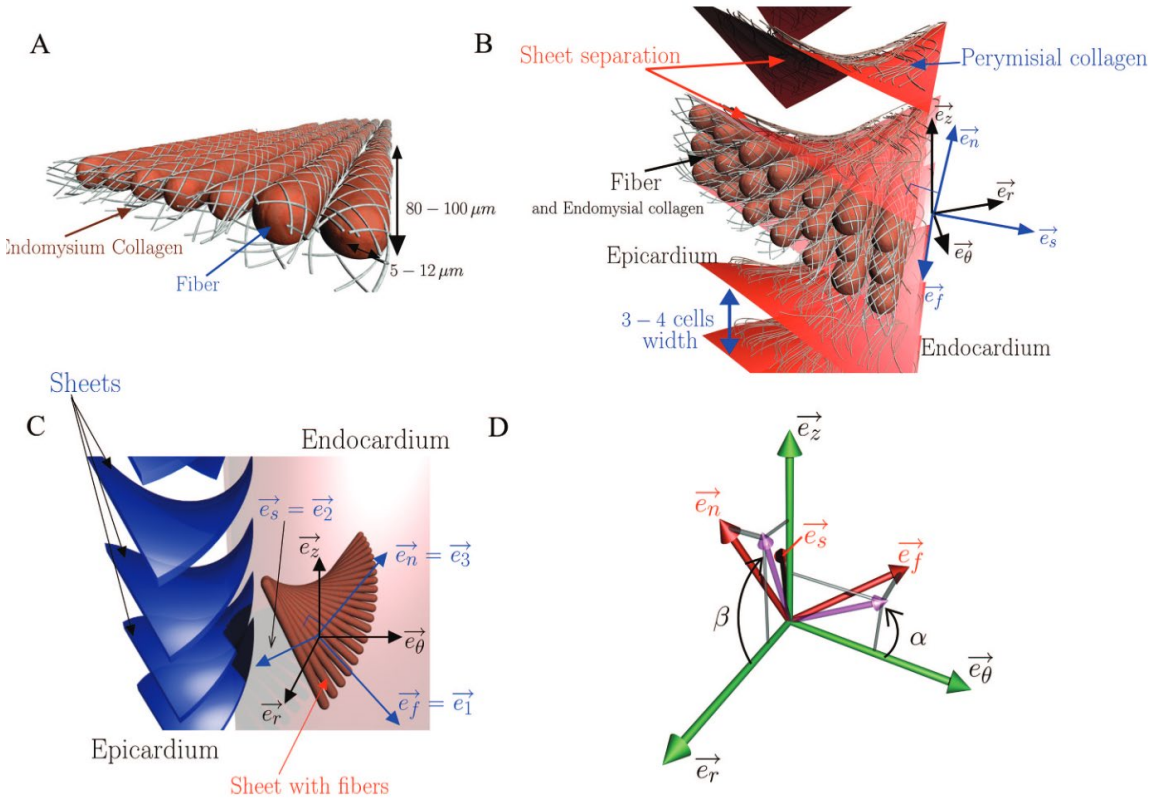

Figure 1.2 Fiber architecture of normal human heart. Adapted with permission from Rohmer et al., 2007**.**

Myocardial disarray consists of a significant derivation in organization from the aforementioned fiber structure. Specifically, the parallel arrangement of myofibers within the sheets is distorted and deviates from the local mean fiber orientation. This disorganization can occur at three levels: macroscopic (between "bundles" of myofibers), light microscopic (intercellular disorganization), and electron microscopic (intracellular/sarcomeric disorganization). In this work, myocardial disarray, also called myocyte disarray, refers primarily to disorganization between myocytes. Figure 1.3 shows examples of structural disorganization at the cellular level.

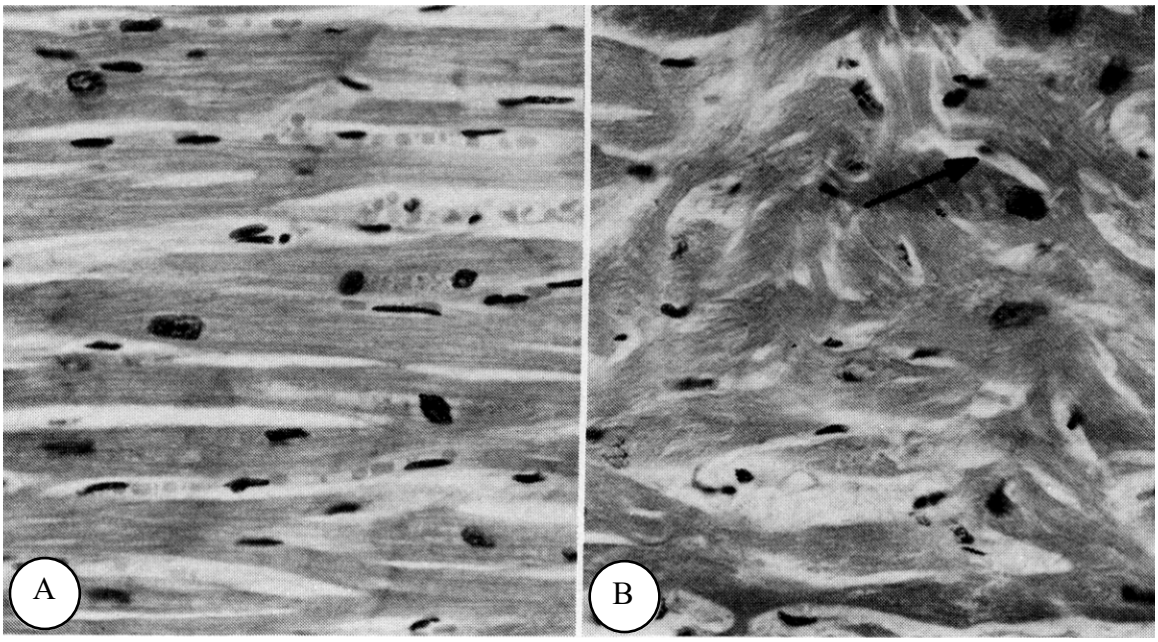

Figure 1.3 Samples of intercellular disarray compared with normal myocyte organization. (A) normal cardiomyocyte organization, and (B) myocyte disarray. Adapted with permission from Bulkley, Weisfeldt, & Hutchins (1977). Note that the disarrayed sample characterizes the fiber organization in the transitional areas (RV junction, LV junction, and trabeculae) of a normal human heart as well as in HCM patients.

1.2 Myofiber Disarray in Hypertrophic Cardiomyopathy

Myofiber disarray frequently develops as a phenotype in a variety of cardiac pathologies is but particularly associated with familial hypertrophic cardiomyopathy (HCM). Familial HCM is an inherited cardiac disease affecting an estimated 1 in 500 people in the general population (Maron, 2002). Although generally characterized by septal hypertrophy, myocyte disarray, interstitial collagen deposition, and small vessel disease, the causal mutations and phenotypic expressions vary considerably among patients. Likewise, clinical outcomes vary broadly as well, from sudden death and end-stage heart

failure to unaffected quality of life in mildly symptomatic patients and non-symptomatic gene carriers. The heterogeneity in genetic mutations, expression, and outcome consequently impairs the identification of high-risk individuals as well as the efficacy of the limited treatment options (Maron, 2002).

Myofiber disarray is considered as a hallmark phenotype in the diagnosis of hypertrophic cardiomyopathy (van der Bel-Kahn, 1977; Maron et al., 1981; Varnava, 2000). In fact, disarray present in 10% of the ventricular myocardium along with other characteristic pathological features, is the standard metric for confirming a diagnosis of HCM (Maron et al., 1981; Davies, 1984). Disarray has been observed to develop in the midwall region of the septum as well as of the posterior and anterior regions (Maron, Anan, & Roberts, 1981; Kuriyabashi & Roberts, 1992). Although disarray can occur in the absence of fibrosis, Kuriyabashi & Roberts (1992) observed that fibrosis was generally present in HCM hearts where myofiber disarray was also present. Particularly, young patients in which the initial manifestation of HCM was sudden death show little to no interstitial or diffuse fibrosis and an extensive degree of severe disarray.

It is worth noting that myofiber disarray is not exclusively a pathological phenotype. Becker and Caruso (1982) performed a histological study on normal and hypertrophic hearts to discern the effectiveness of using myocardial fiber disarray as a distinguishing phenotype in the diagnosis of hypertrophic cardiomyopathy and found that disarray was found in normal hearts in the apical region and at points of transition in the heart, e.g. at the RV insertion points and the subaortic septal region. However, a comparatively high degree of regularity was observed in the midsegment of the septum, in

agreement with other histological studies (Kuriyabashi & Roberts, 1992), irrespective of the orientation of the block of cardiac tissue under observation.

A solid consensus has yet been reached concerning the mechanism by which myofiber disarray develops in patients with hypertrophic cardiomyopathy. Some hold that the development of disarray is related to stress patterns in the heart. Adomian and Beazell (1986) altered the electric pacing in 12 dog hearts to study the effect of altered contraction patterns on myofiber and myofibrillar architecture. They found that 9 out of 12 dog hearts expressed severe disarray (fibers oriented at angles 60 to 90 degrees to each other) in sampled regions from the apex and base of the LV free wall and the mid septum. Sedmera (2005) traced the evolution of myocardial fiber orientation and corresponding activation and contractile patterns through the developmental stages of the heart. In the tubular heart stage, activation follows the flow of the blood through the heart, and myofibrils are oriented circumferentially with no transmural angle. However, as the heterogeneities in activation, and thereby contraction, are introduced, spiraling and transmural angle deviations in myofiber orientation develop. The results of both of these works suggest the response to changing stress patterns as a driver for myocardial fiber reorientation.

1.3 Review of Fiber Reorientation Models

The efforts to develop and incorporate the remodeling of myofibers into physiological and pathological FE cardiac models is limited. To explore possible mechanisms of reorientation, researchers began to optimize fiber orientations to achieve sufficient global function (Arts, Renamen, and Veenstra, 1979; Arts et al., 1982; Rijcken et al., 1997; Bovendeerd et al., 1999) (see review on cardiac growth and remodeling from

Bovendeerd (2012) for more details on optimization approach). The optimization models use global parameters to evolve the orientation of the fibers. However, there is no physiological mechanism by which cardiomyocytes are aware of global cardiac function, and thus an optimization approach is ill-suited to recapitulate the remodeling of cardiac fibers. Instead, myocytes respond to local stimuli, mechanical or otherwise, in the reorientation process.

The first model to publish a local adaptation model was from Arts et al. (1994) in which the fibers were reoriented with a "mismatch" calculation based on sarcomere length and fiber shortening. When compared with experimental data from various animal heart models, the distribution of transmural fiber angles throughout the LV wall model were reasonably similar. Kroon et al. (2009) introduced a strain-based adaptation law with the assumption that myocytes orient themselves in order to minimize shear strain experienced in the cell. The reorientation law is given by:

$$\frac{d\boldsymbol{e}_{f,0}}{dt} = \frac{1}{\kappa}\left(\frac{\boldsymbol{U}\cdot\boldsymbol{e}_{f,0}}{\left|\boldsymbol{U}\cdot\boldsymbol{e}_{f,0}\right|} - \boldsymbol{e}_{f,0}\right)$$

where $\boldsymbol{e}_{f,0}$ is the fiber direction in the reference configuration, which corresponds to the unloaded ventricle state, κ is the adaptation time constant, and $\boldsymbol{U}$ is the right stretch tensor. The model predictions for helix and transverse angles throughout the wall fell within the physiological ranges observed in goat hearts by Bovendeerd at el., 2002. Washio et al. (2016) presented adaptative models based on local muscle workload and contractile load impulse to control reorientation and found load impulse to be a suitable mechanism for fiber reorientation. The impulse-based reorientation law was further refined and tested in physiological and pathological cases in a later work (Washio et al., 2020), with a high

degree of agreement with experimental observations in human hearts. Reorientation was performed during the isovolumetric contraction phase, rather than as a continuous adaptation, to compensate for large simulation times.

The aim of this work is to develop a reorientation law capable of continual adaptation that can reproduce myofiber disarray observed in patients with familial HCM. We hypothesize that myofiber disarray develops in response to heterogeneities in contraction and/or passive properties, i.e. the development of fibrosis, caused by gene expressions associated with familial hypertrophic cardiomyopathy. A stress-driven reorientation law is proposed to model the development of myofiber disarray in the methods section of this thesis (Chapter 2) and studied in different geometries and under varying loading conditions. The results of these studies will be examined in Chapter 3, and a discussion of the virtues and limitations of this work will be presented in Chapter 4. Conclusions and future work will be presented in Chapter 5.

.

CHAPTER 2. METHODOLOGY

2.1 Relevant Continuum Mechanics

Let $\boldsymbol{R_0}$ be the reference configuration of the model geometry and $\boldsymbol{X}$ be the initial position of a material point within the geometry at time $t = 0$.The current position of the material point $\boldsymbol{x}$ is mapped from the reference configuration by way of the motion $\boldsymbol{x} = \boldsymbol{\chi}(\boldsymbol{X},t)$. Utilizing the chain rule, one may ascertain the deformation gradient $\boldsymbol{F}$:

$$d\boldsymbol{x} = \boldsymbol{F}d\boldsymbol{X}. \tag{2.1}$$

where $d\boldsymbol{X}$ is an infinitesimal line element located at the position $\boldsymbol{X}$ in the reference configuration and $d\boldsymbol{x}$ is infinitesimal line element located at the position $\boldsymbol{x}$ in the current configuration. The displacement of the material point is given by:

$$\boldsymbol{u} = \boldsymbol{x} - \boldsymbol{X}. \tag{2.2}$$

Given some displacement $\boldsymbol{u}$ from the initial state $\boldsymbol{X}$, the deformation gradient can be redefined as:

$$\boldsymbol{F} = \boldsymbol{I} + \nabla\boldsymbol{u} \tag{2.3}$$

where $\boldsymbol{I}$ is the identity matrix and $\nabla\boldsymbol{u}$ is the gradient of the displacement field. This definition of $\boldsymbol{F}$ is used for the calculation of the deformation gradient in this modeling approach. The right Cauchy-Green deformation tensor, which is defined as:

$$\boldsymbol{C} = \boldsymbol{F}^{\boldsymbol{T}}\boldsymbol{F} \tag{2.4}$$

enables the calculation of stretch α along a given direction in the reference configuration $\boldsymbol{M}$, given as

$$\alpha^2 = \boldsymbol{M} \cdot \boldsymbol{CM} \tag{2.5}$$

and also the Green strain tensor, defined as:

$$\boldsymbol{E} = \frac{1}{2}(\boldsymbol{C} - \boldsymbol{I}) \tag{2.6}$$

which describes the strain in the model geometry with respect to the reference configuration.

2.2 Modeling of Cardiac Tissue Properties

The bulk material passive properties are modeled as incompressible, transversely isotropic, and hyperelastic using the strain energy function (Guccione, Waldman, & McCulloch, 1993):

$$W_{bulk} = \frac{C}{2}(e^Q - 1) \tag{2.7}$$

where C is a material constant governing isotropic stiffness, which was assigned a value of 266 Pa for normal cardiac tissue and 3130 Pa for fibrotic tissue. Q is defined as:

$$Q = b_f {E_{11}}^2 + b_t\left({E_{22}}^2 + {E_{33}}^2 + {E_{23}}^2 + {E_{32}}^2\right) + b_{fs}\left({E_{21}}^2 + {E_{12}}^2 + {E_{13}}^2 + {E_{31}}^2\right) \tag{2.8}$$

where b_f, bt, and b_{fs} are the transversely orthotropic material constants. Utilizing a local cardiac coordinate system, E_{11}, E_{22}, and E_{33} are the normal components of $\boldsymbol{E}$, with respect to the fiber, sheet, and sheet-normal directions, respectively, and E_{12}, E_{21}, E_{23}, E_{32}, E_{13}, and E_{31} are the shearing components of $\boldsymbol{E}$. To simulate normal cardiac tissue, the material constants b_f, b_t, and b_{fs} were set to 10.48, 3.58, and 1.627, respectively. The fibrotic tissue was assumed to be isotropic. Thus, b_f, bt, and b_{fs} were all set to 10 to capture the isotropic

nature of the fibrotic tissue. The myofiber passive properties are modeled using the strain energy function (Xi, Kassab, & Lee, 2019):

$$W_f = \begin{cases} C_2\left(e^{C_3(\alpha-1)^2}\right), & \alpha > 1 \\ 0, & \alpha \leq 1 \end{cases} \tag{2.9}$$

where C_2 and C_3 are material constants and α is the uniaxial stretch of the myofiber. Values for material constants C_2 and C_3 were set to 172 Pa and 7.6, respectively (Mann et al., 2020).

The cardiac tissue is modeled as a hyperelastic, incompressible material. The passive component of the second Piola-Kirchhoff stress $\boldsymbol{S}$ is given through the constitutive relationship

$$\boldsymbol{S}_{passive} = \frac{\partial W_f}{\partial \boldsymbol{E}} + \frac{\partial W_{bulk}}{\partial \boldsymbol{E}} - p\boldsymbol{C}^{-1} \tag{2.10}$$

where p is the hydrostatic pressure, which is determined via a Lagrange multiplier, as described in a later section.

The contractile properties of the cardiac tissue were represented using a model of sarcomere-level contraction, called MyoSim, developed by Campbell et al. (2014). Briefly, the MyoSim model uses cross-bridge distributions and myosin kinetics to calculate the force generated by a single myocyte. In the three-state kinetic scheme (Mann et al., 2020), the myosin heads in the model exist in one of three populations: the super-relaxed (SRX) state, the disordered-relaxed (DRX) state, or the force-generating (FG) state. A set of coupled ordinary differential equations, which describe the myosin kinetics, are solved to determine the distribution of heads in each population. Once the population of myosin heads in the FG population is known, the active stress in the fiber direction can be

calculated. In addition, 25% of the active stress in the myofiber direction was assigned to the cross-fiber (sheet and normal) directions to mimic the transverse transmission of active stress observed in cardiac tissue. Tables 2.1 and 2.2. list the parameters used to characterize the contractile properties of the cardiac tissue.

Table 2.1 List of cell ion parameters used in contraction model

Parameter	Value	Units
Calcium content	0.001	Molar
k_{leak}	0.008008008	
k_{act}	1.447218638	
k_{serca}	80	
duration	4.5	ms

Table 2.2 List of myofilament parameters used in contraction model

Parameter	Value	Units	Parameter	Value	Units
$k_{cb,pos}$	0.001	$N\ m^{-1}$	k_{cb}	0.001	$N\ m^{-1}$
$k_{cb,neg}$	0.001	$N\ m^{-1}$	x_{ps}	5.0	nm
α	1.0		k_{on}	5.0E+08	$M^{-1}\ s^{-1}$
k_1	3.0	s^{-1}	k_{off}	200	s^{-1}
k_{force}	0.00051	$m^2\ s^{-1}$	k_{coop}	3.38	
k_2	200	s^{-1}	bin range	[-10,10]	nm
k_3	330	$nm^{-1}\ s^{-1}$	bin width	1.0	nm
$k_{4,0}$	258.864648098	s^{-1}	$k_{falloff}$	0.0024	
$k_{4,1}$	2.089	nm^{-4}			

2.3 Stress-based Reorientation Law

We begin by defining the relationship between the first Piola-Kirchhoff stress tensor, $\boldsymbol{P}$, and the second Piola-Kirchhoff stress tensor, $\boldsymbol{S}$, which is given by $\boldsymbol{S} = \boldsymbol{F^{-1}P}$. We also note the relationship between the first Piola-Kirchhoff traction vector and stress

tensor, which is given by $\boldsymbol{p}_{(\boldsymbol{N})} = \boldsymbol{PN}$. For convenience with respect to the finite element implementation, we recast the referential eigenproblem using the second Piola-Kirchhoff stress tensor:

$$(\boldsymbol{S} - S\boldsymbol{I})\boldsymbol{N} = 0 \tag{2.11}$$

where $\boldsymbol{N}$ is the normal unit vector to a plane as defined in the reference configuration and S is scalar value. We define a reference traction vector, with respect to the second Piola-Kirchhoff stress tensor, which is given by:

$$\boldsymbol{s}_{(\boldsymbol{N})} = \boldsymbol{SN} = \boldsymbol{F}^{-1}\boldsymbol{p}_{(\boldsymbol{N})} \tag{2.12}$$

This traction vector can be separated into normal and shear components. By projecting the traction vector onto the normal vector $\boldsymbol{N}$, the normal component of the traction vector, given as:

$$\left(\boldsymbol{s}_{(\boldsymbol{N})} \cdot \boldsymbol{N}\right)\boldsymbol{N} = \boldsymbol{s}_{(\boldsymbol{N})}(\boldsymbol{N} \otimes \boldsymbol{N}) \tag{2.13}$$

can be recovered. The shear component of the traction vector is then given by:

$$\boldsymbol{s}_{(\boldsymbol{N})} - \left(\boldsymbol{s}_{(\boldsymbol{N})} \cdot \boldsymbol{N}\right)\boldsymbol{N} = \boldsymbol{s}_{(\boldsymbol{N})}(\boldsymbol{I} - \boldsymbol{N} \otimes \boldsymbol{N}) \tag{2.14}$$

By rewriting Equation 2.11 using Equations 2.13 and 2.14, it can be shown that

$$\boldsymbol{s}_{(\boldsymbol{N})}(\boldsymbol{I} - \boldsymbol{N} \otimes \boldsymbol{N}) = 0 \tag{2.15}$$

must be true if $\boldsymbol{N}$ is an eigenvector of the referential stress tensor. In other words, alignment with the direction of maximum normal traction minimizes the shear stresses in the planes characterized by the eigenvector solutions. Likewise, for the stretch eigenproblem

$$(\boldsymbol{U} - \lambda \boldsymbol{I})\boldsymbol{M} = 0 \tag{2.16}$$

where λ are the principal stretches and $\boldsymbol{M}$ are the principal stretch directions (eigenvectors), the stretch is maximized along the direction of the first eigenvector. It can also be shown that the associated eigenvectors for the stretch eigenproblem are identical to those for the Green strain eigenproblem.

Kroon et al. (2009) sought to maximize the stretch experienced by the myofiber during the reorientation process. The stress reorientation law we developed takes inspiration from Kroon's stretch-based law, as shown in Eq. 1.1, and the insights from the referential stress eigenproblem. The reorientation is defined such that the principal stress direction is sought by determining the maximum normal traction direction for the referential stress tensor and comparing it to the reference fiber direction at a given time. The stress reorientation law is given as:

$$\frac{d\boldsymbol{e}_{f,0}}{dt} = \frac{1}{\kappa}\left(\frac{\boldsymbol{S}\boldsymbol{e}_{f,0}}{\left\|\boldsymbol{S}\boldsymbol{e}_{f,0}\right\|} - \boldsymbol{e}_{f,0}\right) \tag{2.17}$$

where $\boldsymbol{e}_{f,0}$ is the fiber unit vector in the reference configuration and κ is a time constant. The rate of change in the reference fiber direction vanishes when the fiber direction is aligned with the direction of maximum normal traction for a given referential stress state. This condition satisfies Eq. 2.15.

Because the referential stress tensor is formulated as a sum of its passive and active components, it is possible to direct the reorientation law with either component of the referential stress as well as with the total stress. Thus, the driving component of the referential stress was specified at the onset of each simulation and used as the stress tensor

in the reorientation law. For select simulations, reorientation was driven by the active stress component, the passive component, or the total stress for a given mesh and set of tissue properties, and the resulting final orientations were compared. The reorientation obtained from the stretch-based law was performed and compared to the stress-based results for each simulation. To avoid the computational burden associated with the calculation of the right stretch tensor $\boldsymbol{U}$, the right Cauchy-Green deformation tensor was used for the stretch-based reorientation. The reorientation law was implemented such that the reference fiber direction was updated at the end of each timestep throughout the simulation.

2.4 Finite Element Modeling

We constructed several mesh geometries in which to investigate the properties of the stress-based reorientation law. The meshes are created using functions from FEniCS 2019.1.0 (Chalmers University of Technology, Göteberg, Sweden). All simulations used second-order, Lagrangian tetrahedral elements with four integration points per element to create the mesh.

2.4.1 Uniaxial and Simple Shear Simulations

The unit cube mesh was created for the performance of uniaxial and simple shear simulations (see Figure 2.1a). The unit cube geometry consists of 6 elements. The fiber direction $\boldsymbol{e}_{f,0}$ was initialized along the x-axis, and the time constant was set to 5 ms. Constraints were placed on the left (x = 0), back (z = 0), and bottom (y = 0) faces such that the faces remained in plane while allowing the Poisson effect to occur. A fixed-point boundary condition was placed at the origin to prevent rigid body translation. A displacement boundary condition was placed on the right face to induce the desired

deformations. The cube was stretched 11.5% of its original length along the x-axis over 5 timesteps for the uniaxial simulation. In the simple shear simulation, the same displacement was applied in the y-direction over 5 timesteps. Figure 2.2 shows the final deformations for the uniaxial and simple shear simulations.

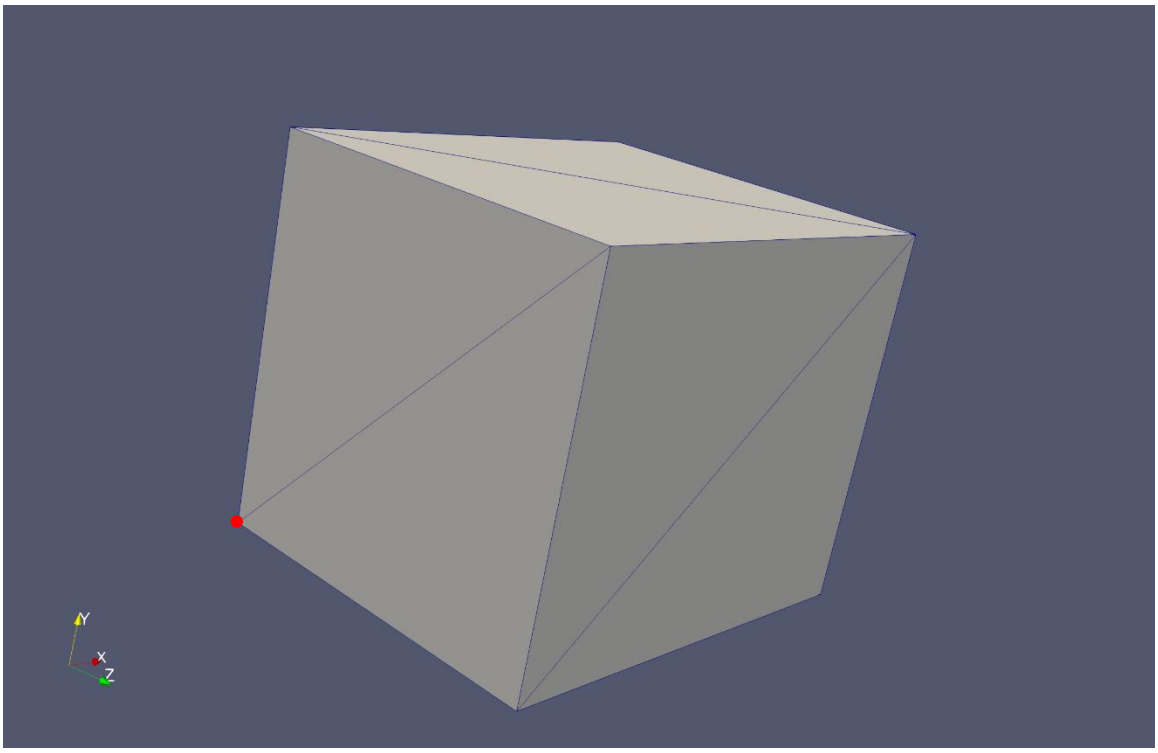

Figure 2.1 Mesh configuration for uniaxial and simple shear simulations. The red point marks the origin (0,0,0) on the back face of the unit cube. Mesh rendered in ParaView 5.7.0 (Kitware, Clifton Park, NY).

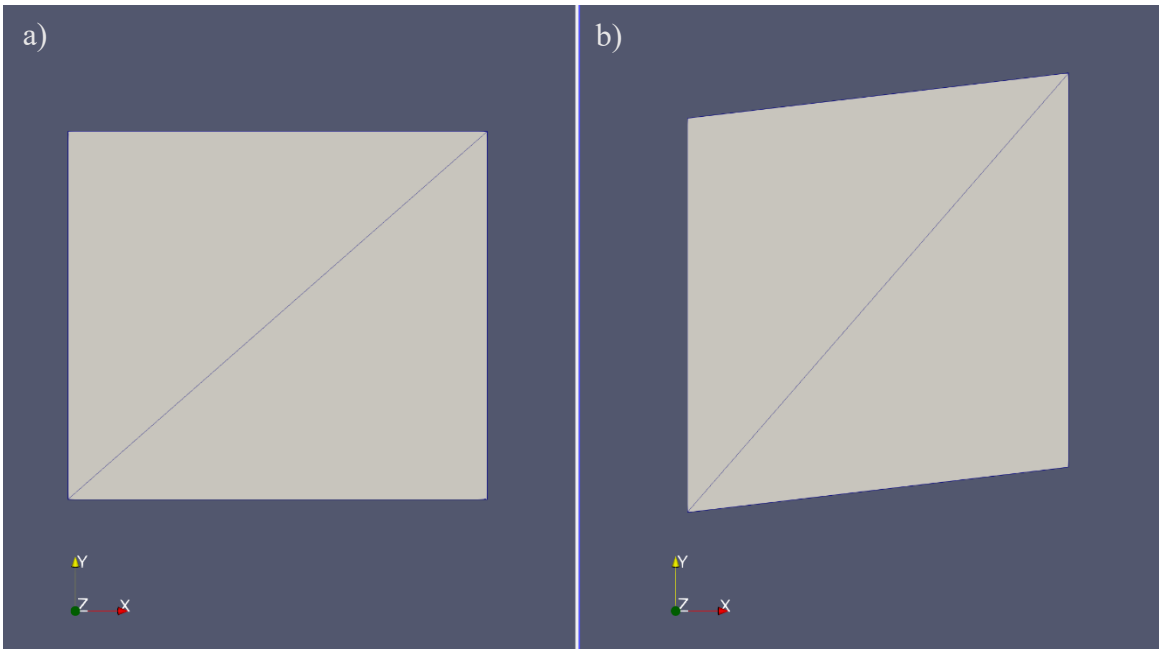

Figure 2.2 Final deformations for the uniaxial and simple shear simulations. (a) Final deformation for the uniaxial simulations, and (b) final deformation for the simple shear simulations. Mesh rendered in ParaView 5.7.0.

2.4.2 Inclusion Simulations

Figure 2.3 shows a cross-sectional view of the mesh for the inclusion simulation. The mesh represented an inclusion of fibrotic material within a block of normal cardiac tissue where the inclusion is a unit cube in the center of a larger 3x3x3 cube. The cube was subjected to the same uniaxial loading conditions described in the unit cube uniaxial simulation above. The fiber direction was initialized along the x-axis, and the time constant was set to 10 ms. Reorientation in the fibrotic region was disabled. The boundary conditions were also identical to those applied in the uniaxial and simple shear simulations.

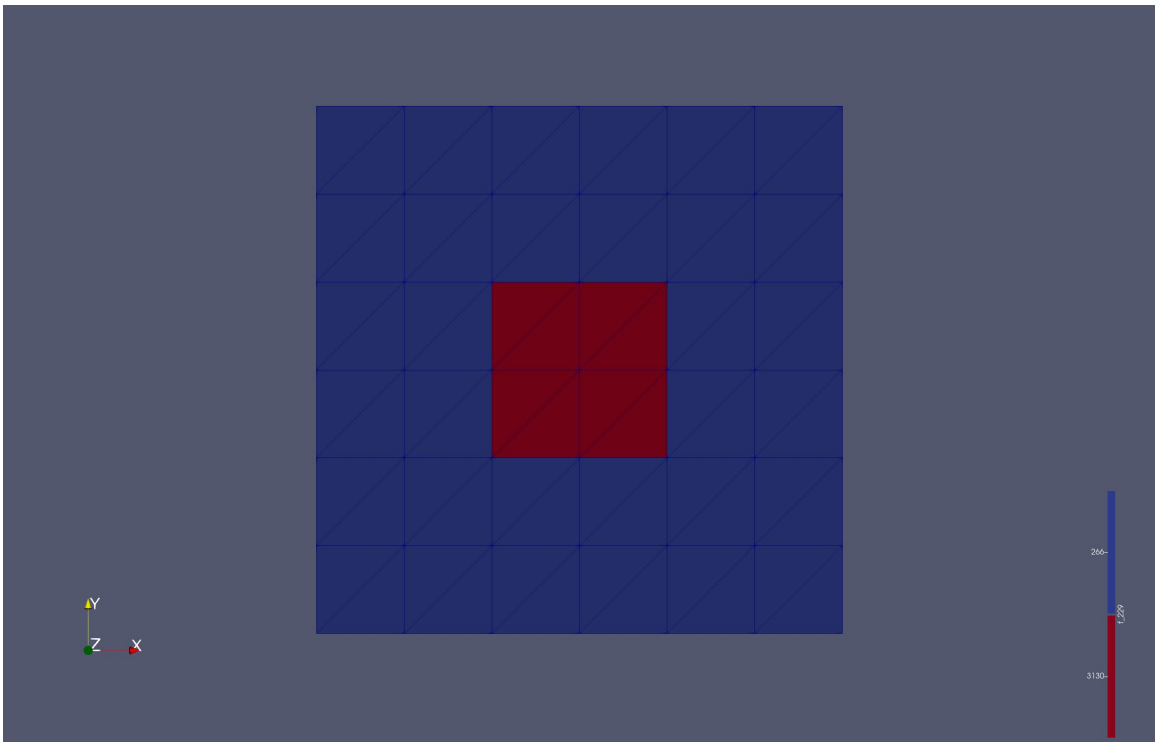

Figure 2.3 Cross-sectional view of the mesh configuration for inclusion simulation. The red region represents the fibrotic inclusion, and the blue region represents normal cardiac tissue. Mesh rendered in ParaView 5.7.0.

2.4.3 Heterogeneous Strip Simulations

A rectangular box mesh was used to represent a strip of cardiac tissue with varying passive and contractile properties. The mesh consisted of 1920 tetrahedral elements for this model. The time constant was set to 240 ms to ensure that reorientation occurred over several cardiac cycles. Ten percent of the strip geometry at the left end was considered to be compliant with respect to the rest of the tissue and was modeled with a reduced isotropic stiffness value of C = 26.6 Pa. The cross-bridge density was set to 0 in order to eliminate contraction in the compliant region.

For each of the strip simulations, the strip was subjected to cyclical loading conditions designed to mimic the cardiac cycle. A traction boundary condition on the right face of the strip was ramped up to a magnitude of 4000 Pa over 75.0 ms to mimic passive diastolic loading. Once the prescribed traction was reached, the displacement of the right face was held constant as isometric contraction occurred in the tissue. Upon exceeding a load of 30 kPa, the strip was allowed to shorten against a prescribed traction (afterload) of 30 kPa. When shortening was completed, the displacement of the right face was fixed again until full relaxation was achieved. Fiber adaptation was disabled in the fibrotic and compliant regions and for the first cycle of the strip simulations in order to obtain reference data for analysis.

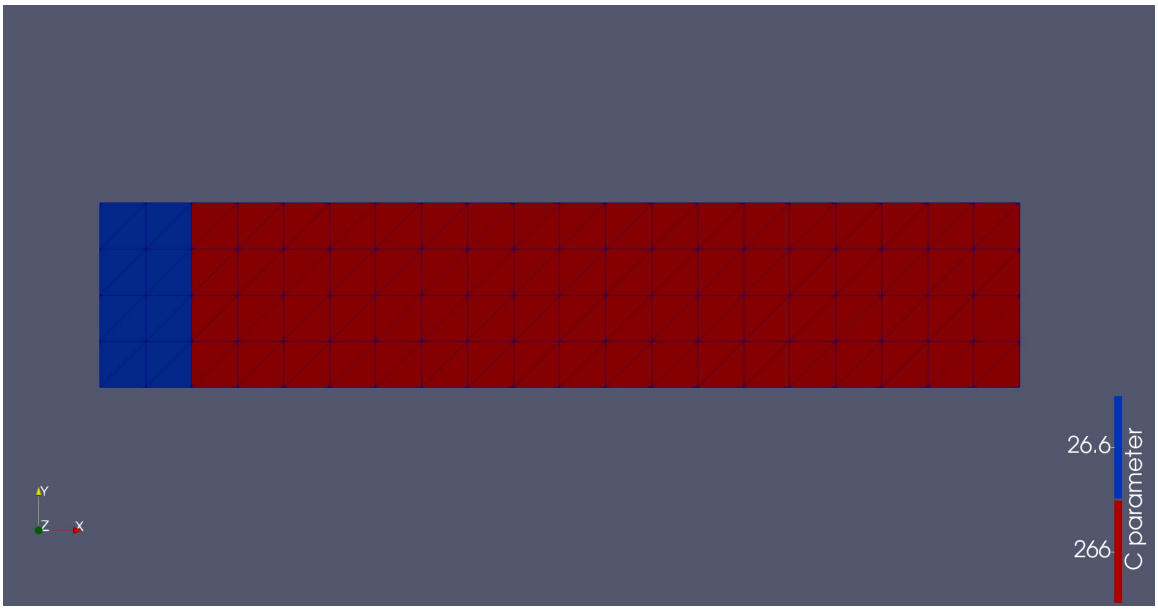

Figure 2.4 Mesh configuration for homogeneous strip simulation. The compliant end is represented in blue, and the normal cardiac tissue is represented in red. Mesh rendered in ParaView 5.7.0.

2.4.3.1 Interstitial Fibrosis Simulations

To determine whether interstitial fibrosis could be a potential cause of myocardial disarray, 40% of the simulated cardiac tissue in the strip geometry was designated as fibrotic tissue. These elements were randomly selected using a random sampler function from NumPy 1.16.6 and assigned the passive parameters correspondent to fibrotic tissue. The mesh configuration with the selected fibrotic elements is shown in Figure 2.5.

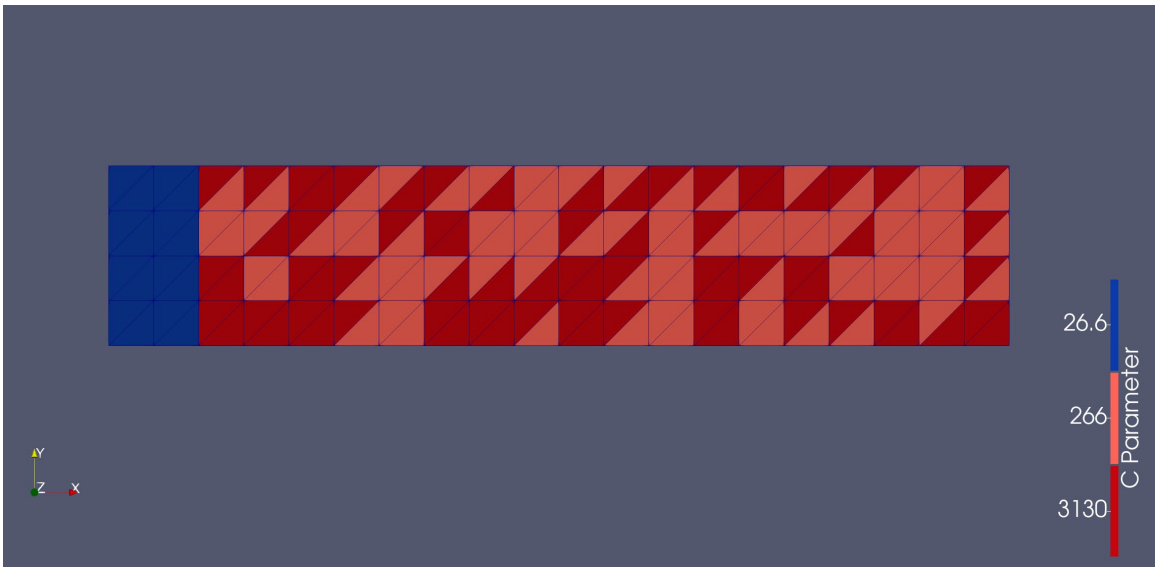

Figure 2.5 Mesh configuration for the interstitial fibrosis strip simulation. The blue region represents the compliant end, the light red regions represent normal cardiac tissue, and the dark red regions represent fibrotic, non-contracting elements. Mesh rendered in ParaView 5.7.0.

2.4.3.2 Heterogeneous Contractility Simulations

It has been suggested that myocyte disarray in HCM patients could be caused by heterogeneities in contraction among neighboring myocytes (Kraft et al., 2013; Kraft & Montag, 2019). To test the potential of contractile heterogeneities as a cause of myocardial disarray, a uniaxial strip simulation with heterogeneous contractile properties was

performed. Forty percent of the elements were designated as tissue with impaired contraction. The mean value of the cross-bridge densities in the impaired tissue was adjusted to 5.081E16 cross bridges per m^2 with a standard deviation of 2.692E16 cross bridges per m^2. The value for each impaired element was selected randomly from a normal distribution truncated at [1.829E14 (-1.88SD), 2.088E17 (3SD)] with the mean and standard deviation given above to prevent the selection of negative cross-bridge values. The distribution of cross-bridge densities overlaid with the mesh configuration is presented in Figure 2.5. The total stress ***S*** was used to adapt the fiber orientations in this simulation.

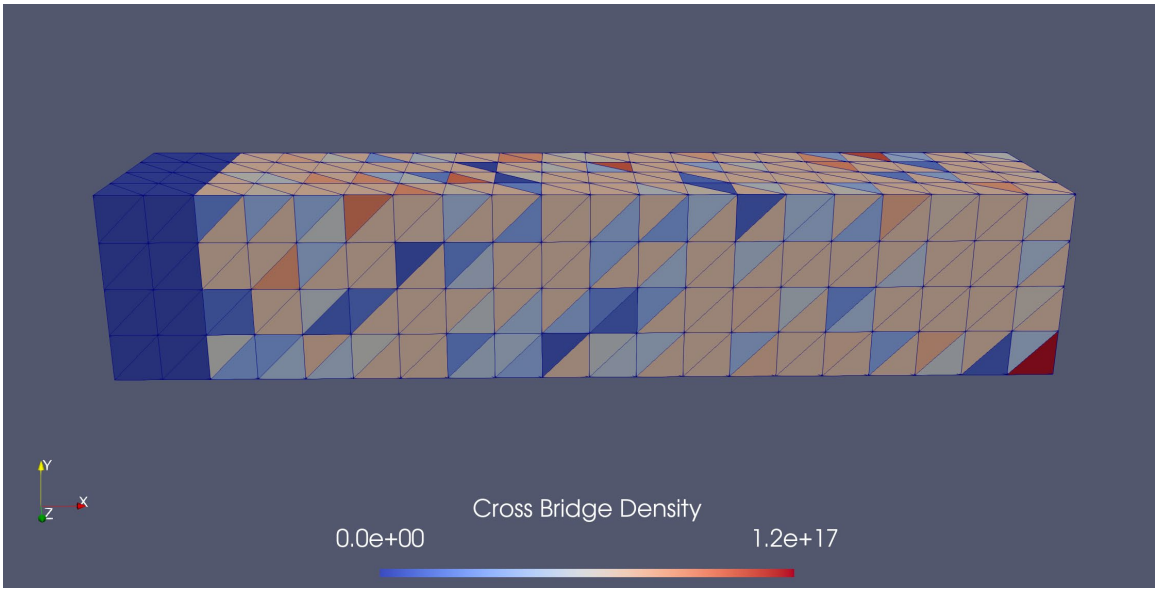

Figure 2.6 Mesh configuration for impaired contraction strip simulation. The color bar represents the range of cross-bridge densities present in the strip simulation. Mesh rendered in ParaView 5.7.0.

2.5 Data Analysis

Myocyte disarray was represented as a distribution of deviations from the initial fiber direction along the x-axis. A custom code was created to analyze and display the fiber

distributions using Python 2.7.18 (PSF, Wilmington, DE). Fiber orientations were visualized in ParaView 5.7.0. Referential shear stress data were recorded at each timestep and plotted using the Data Analysis tool in ParaView. The maximum shear stress before reorientation was compared to the maximum shear stress for the last full cycle to calculate shear stress reduction.

CHAPTER 3. RESULTS

3.1 Uniaxial and Simple Shear Simulations

A comparison between stress- and strain-based reorientation with two initial orientations (0^o, 45^o) was conducted to establish a basic understanding of the behavior of the stress-based reorientation law. This comparison was performed for uniaxial and simple shear loading simulations. When the fiber direction was initialized along the direction of uniaxial loading, i.e. along the x-axis, no reorientation occurred under either stress-based or strain-based reorientation. When the fibers were offset at 45 degrees, reorientation occurred towards the x-axis in the uniaxial simulations. A stress-to-strain comparison of the deformations at the start of reorientation (t = 6 ms) and the end of the uniaxial simulation with 45-degree fiber offset is shown in Figure 3.1. Both the reorientation laws result in similar final orientations and deformations. Similarly, there was no significant difference in final orientation among the simple shear simulations, despite differences in initial orientation and reorientation law.

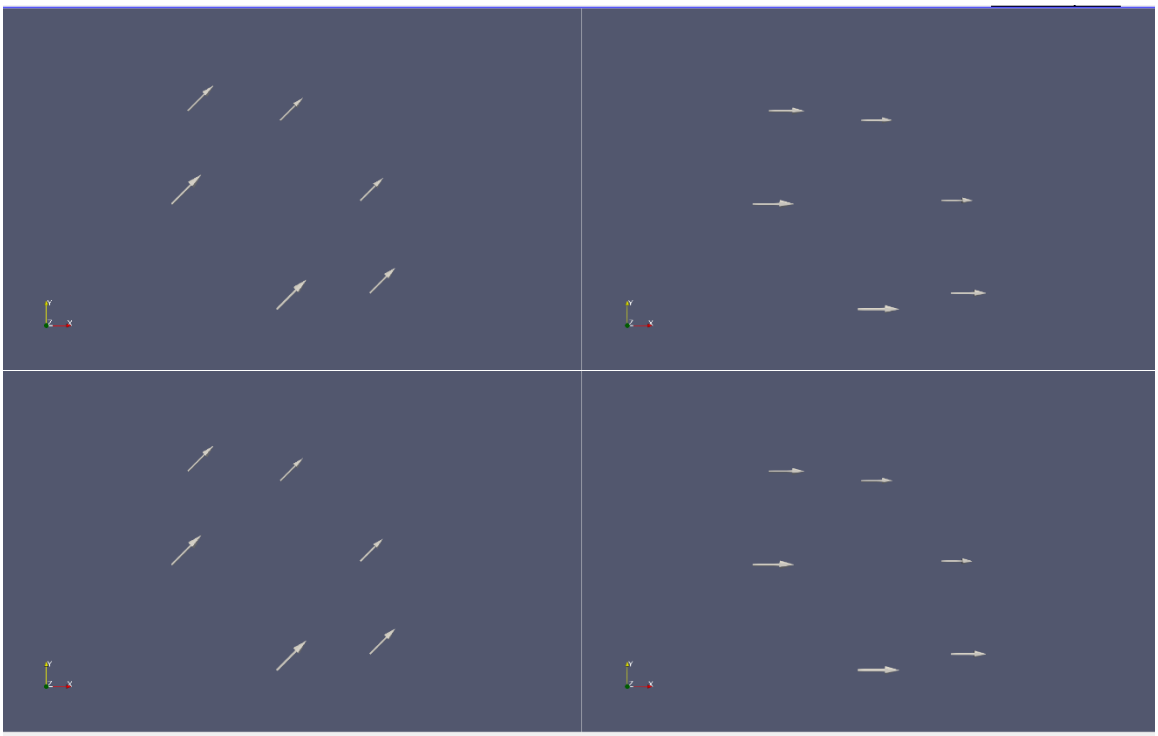

Figure 3.1 Fiber orientations at the start and end of the uniaxial, 45-degree fibe offset simulations. Top row: strain-based adaptation; Bottom row: stress-based adaptation. Glyphs rendered in ParaView 5.7.0.

The average magnitudes of τ_{fs}, τ_{fn}, and τ_{sn} for the stress and strain-based reorientations under uniaxial loading are shown in Figure 3.2. The fiber-sheet shear stress τ_{fs} is given by

$$\tau_{fs} = \boldsymbol{e}_{s,0} \cdot \boldsymbol{S}\boldsymbol{e}_{f,0} \tag{3.1}$$

where $\boldsymbol{e}_{s,0}$ is the sheet unit direction in the reference configuration. Similarly, the sheet-normal shear stress τ_{sn} is given by

$$\tau_{sn} = \boldsymbol{e}_{n,0} \cdot \boldsymbol{S}\boldsymbol{e}_{s,0} \tag{3.2}$$

where $\boldsymbol{e}_{n,0}$ is the normal unit direction in the reference configuration, and the fiber-normal shear stress is given by

$$\tau_{fn} = \boldsymbol{e}_{n,0} \cdot \boldsymbol{S}\boldsymbol{e}_{f,0}. \tag{3.3}$$

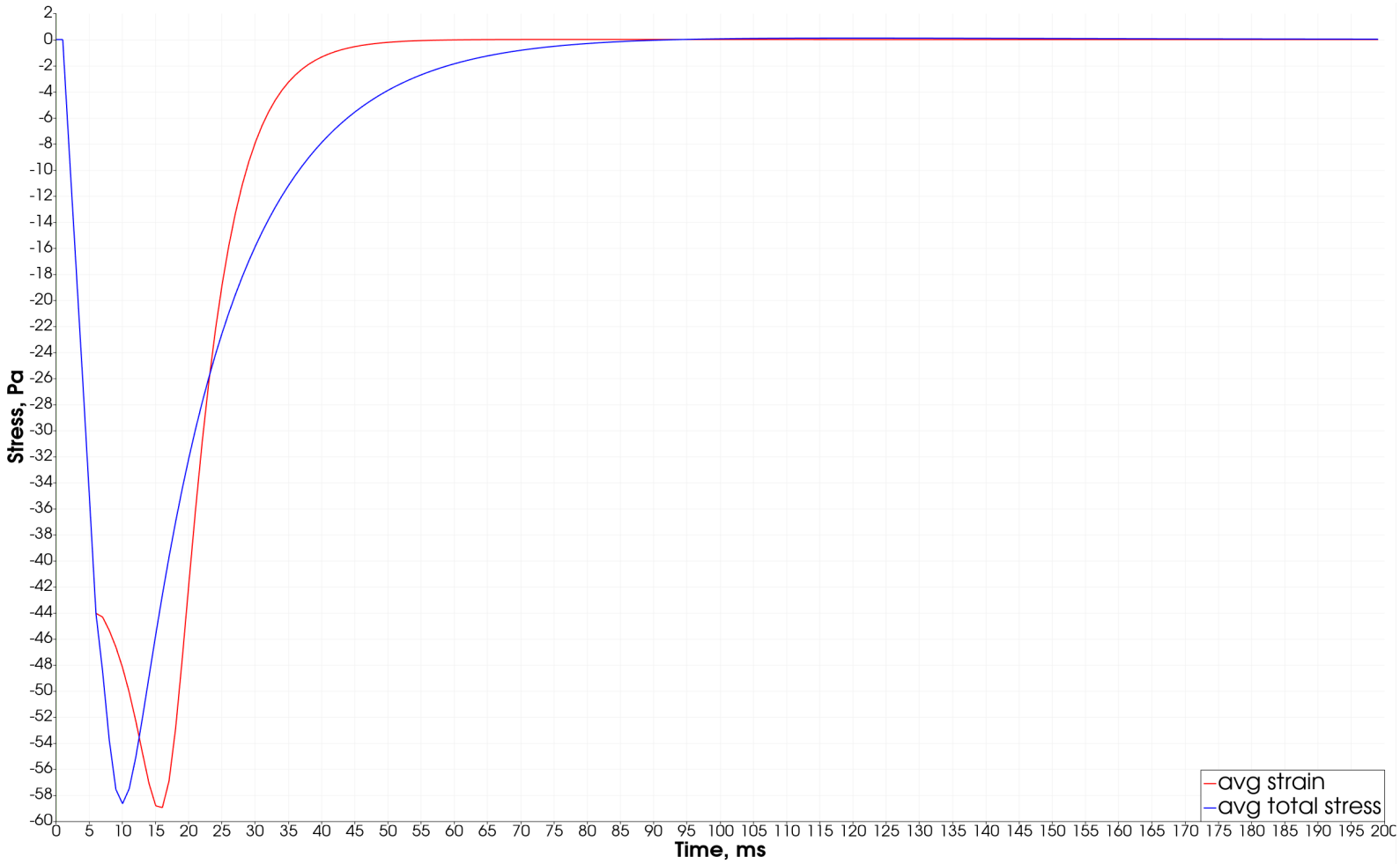

Figure 3.2 Average magnitudes of fiber-sheet shear stresses (in Pa) in uniaxial simulations over time (in ms). Plot rendered in ParaView 5.7.0.

Interestingly, the average magnitudes of τ_{fs}, τ_{fn}, and τ_{sn} all increase in the first 5 timesteps after the beginning of reorientation, after which the shear stresses decrease towards zero by the end of the simulation. All of the shear stress magnitudes approached zero as the simulation progressed. The strain-based reorientation was complete at t = 53.0 ms, whereas the stress-based reorientation was complete at t = 113.0 ms.

Additional simulations were run to investigate the effects of initial fiber orientation and boundary conditions on the stress-based reorientation law, as shown in Table 3.1. Fibers initialized at 225 degrees resulted in a final orientation along the x-axis opposite than that of fibers initialized at 45 degrees, suggesting that there is more than one solution for a given set of boundary and loading conditions. When the fibers were initialized orthogonal to the x-axis, the location of the fixed-point boundary condition affected the final orientations of the fibers. Locating the fixed point at the origin produced varied final orientations, where two fibers are oriented along the negative x-direction, three along the positive x-direction, and one remaining at 90 degrees. All fibers were aligned along the x-axis when the fixed point was located at (0,1,0) (refer to Figure 2.1 for mesh configuration), with two in the negative x-direction and four in the positive x-direction. At the end of the simulation with the fixed point located at (0,0,1), all fibers were oriented in the positive x-direction.

Table 3.1 Results for Stress-Based Uniaxial Simulations

Initial Orientation (degrees)	Fixed Point (Boundary Conditions)	Final Orientation (degrees)
0	(0,0,0)	0
45	(0,0,0)	0
	(0,0,0)	varied
90	(0,1,0)	varied
	(0,0,1)	0
225	(0,0,0)	180

Figure 3.3 shows the results from the time constant sensitivity studies performed with respect to reorientation completion time. The stress reorientation completion data was fitted with a power function

$$t_{finish} = 39.218\kappa^{0.6545}$$

where t_{finish} is the reorientation completion time, defined as the time at which the change in orientation is less than 0.0001, and κ is the time constant used in the reorientation laws shown in the previous chapter. Similarly, the power function

$$t_{finish} = 14.379\kappa^{0.816}$$

was fitted to the strain reorientation completion data. These functions can be used to approximate the adequate duration for a given simulation to ensure reorientation is achieved.

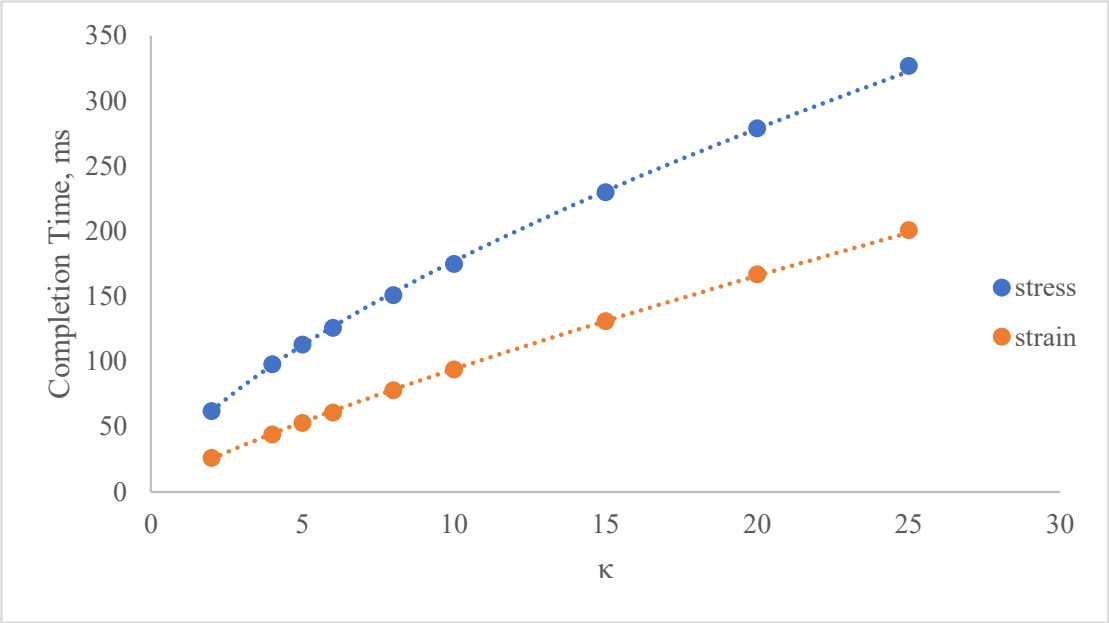

Figure 3.3 Plot of reorientation finish time versus time constant obtained using uniaxial, fiber offset simulations.

3.2 Inclusion Simulations

A simulation was run for each reorientation law with initial orientations of 0 and 45 degrees. Figure 3.4 shows a comparison of the final orientations for the inclusion simulations. Both the stress- and strain-based, 0-degree simulations resulted in minimal reorientation from the x-axis of fibers along the top and bottom of the inclusion. As shown in Figure 3.4, the final fiber orientations for the strain-based, 45-degree offset case was identical to those of the 0-degree simulations. The average fiber-sheet shear strain was -0.00082. Conversely, the final orientations for the corresponding stress-based simulation formed a pattern which was distinctly different, deviating around the inclusion along the 45-degree line in the fiber-sheet plane. The average fiber-sheet shear stress was -18.97 at the end of the simulation.

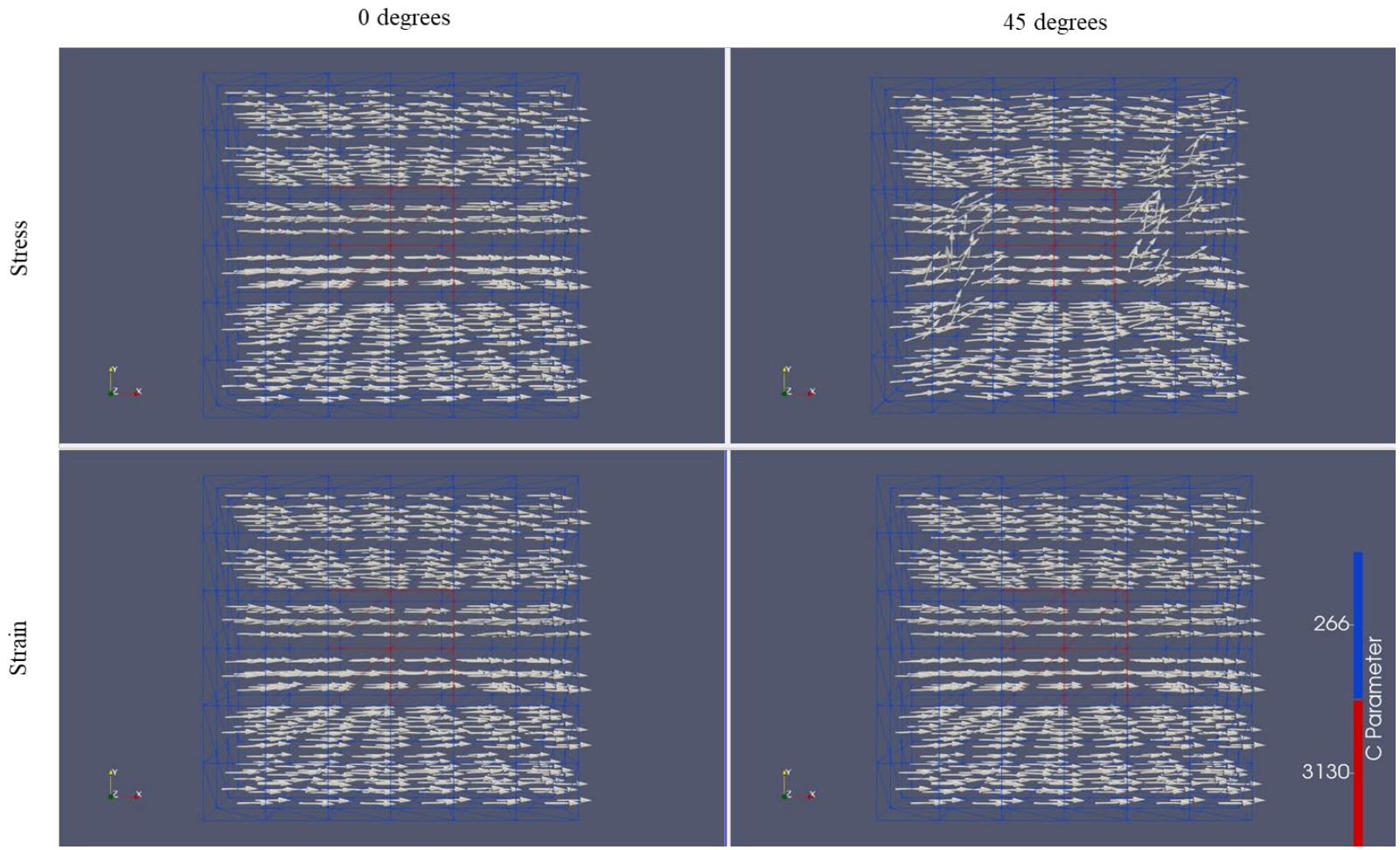

Figure 3.4 Comparison of final fiber orientations by initial fiber angle for the uniaxial simulations. Mesh and glyphs rendered in ParaView 5.7.0.

3.3 Interstitial Fibrosis Simulations

The final fiber orientations for the homogeneous strip simulation are shown in Figure 3.5. None of the reorientation laws resulted in reorientation for the homogeneous strip case, i.e., all of the fibers were aligned with the direction of loading. Figure 3.6 shows the final orientations for the interstitial fibrosis simulations. There was no change in orientation as a result of active stress-based adaptation; the difference in initial and final fiber orientation is 1.421E-14 degrees. Qualitatively, the degree of disorganization which developed as a result of passive stress-based adaptation was similar to that which resulted from stain-based adaptation. Total stress-based adaptation produced notably less disorganization. The large percentage of fibers were oriented within a 1.5-degree deviation from the x-axis at the end of the total stress (45.7%), passive stress (41.6%), and strain (39.5%) simulations. The fibers in the strain simulations showed the greatest deviation from the original orientation along the x-axis.

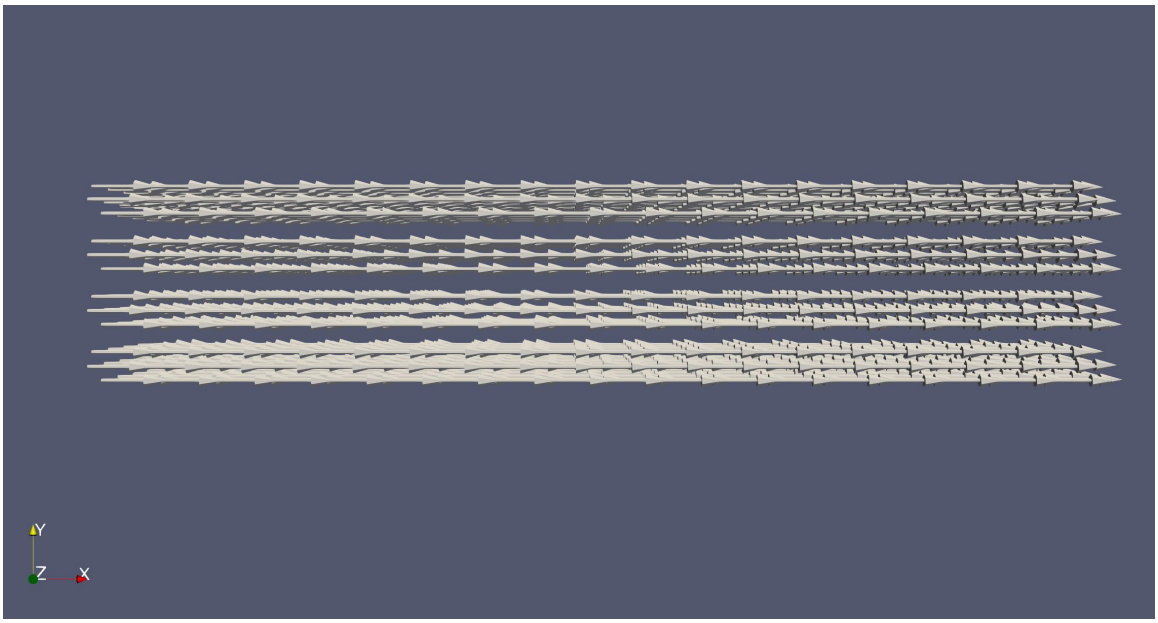

Figure 3.5 Final fiber orientations for homogeneous strip simulation. Glyph rendered in ParaView 5.7.0.

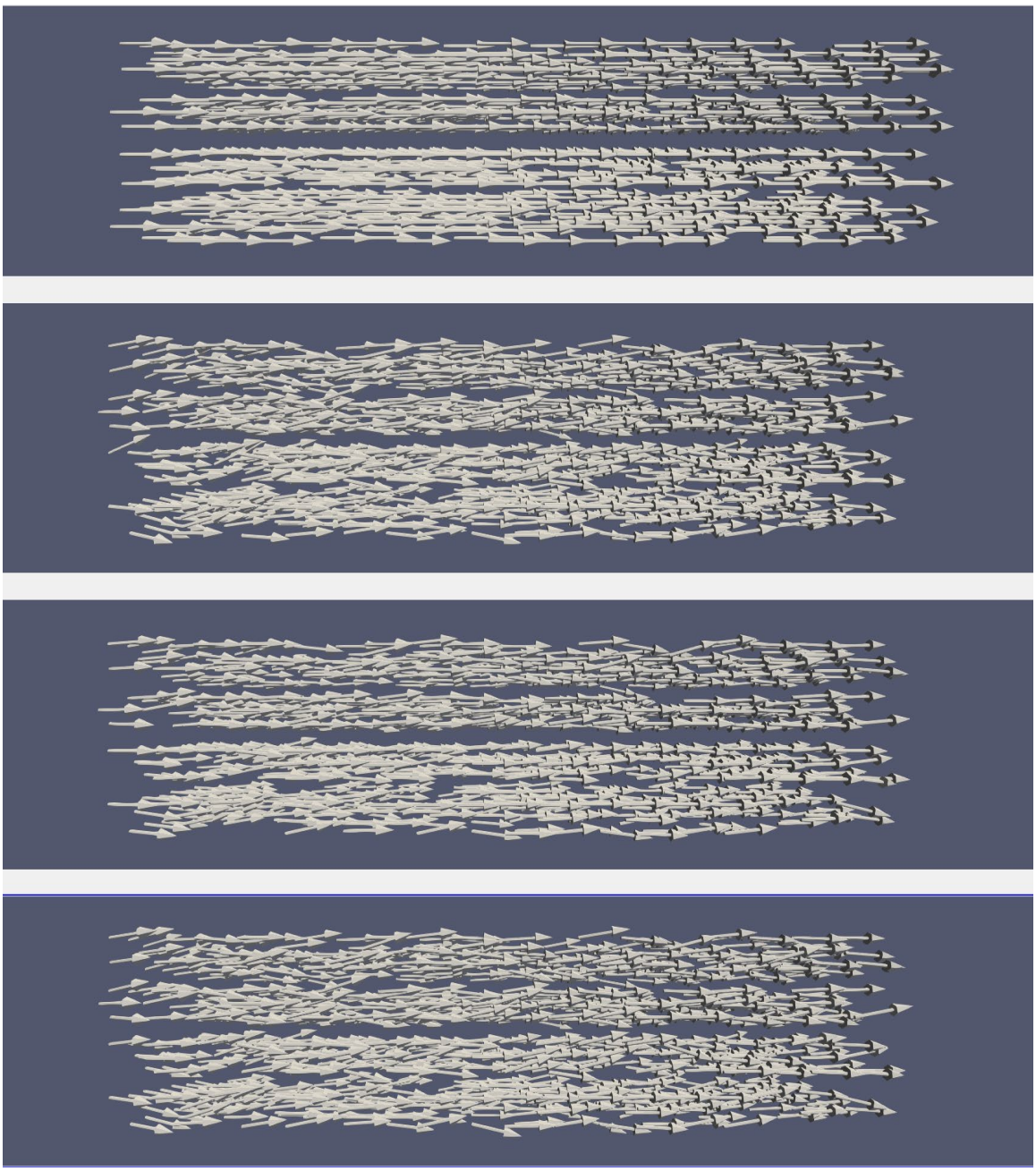

Figure 3.6 Final fiber orientations for the interstitial fibrosis simulations. Top to bottom: active stress-based adaptation, passive stress-based adaptation, total stress-based adaptation, and strain-based adaptation. Note that the final orientations corresponding to the compliant and fibrotic regions are not shown. Glyphs rendered in ParaView 5.7.0.

The fiber-sheet total shear stresses for the passive, total, and strain-based simulations are plotted in Figure 3.7. The maximum shear stress for the first cycle was compared to the maximum shear stress for the last full cycle to calculate shear stress reduction. The maximum shear stress before reorientation was 6939.31 Pa. The strain-based simulation resulted in the greatest reduction in total shear stress (33.76% versus 24.62% [passive], 12.77% [total]).

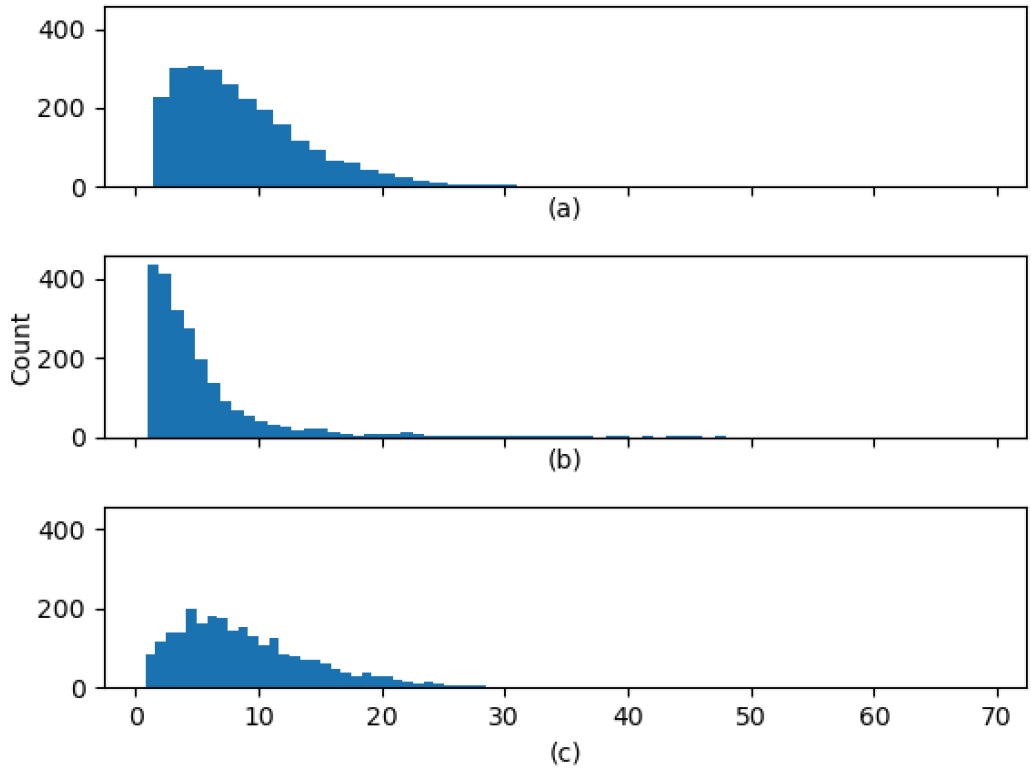

Figure 3.7 Distributions of fiber deviations from the x-axis for reorientation various reorientation laws. a) Passive stress-based, b) total stress-based, and c) strain-based reorientations. Note that only the fibers in the elements representing normal cardiac tissue are shown. The distribution from the active stress-based simulation is not included in the figure, due to the fact that no reorientation occurs.

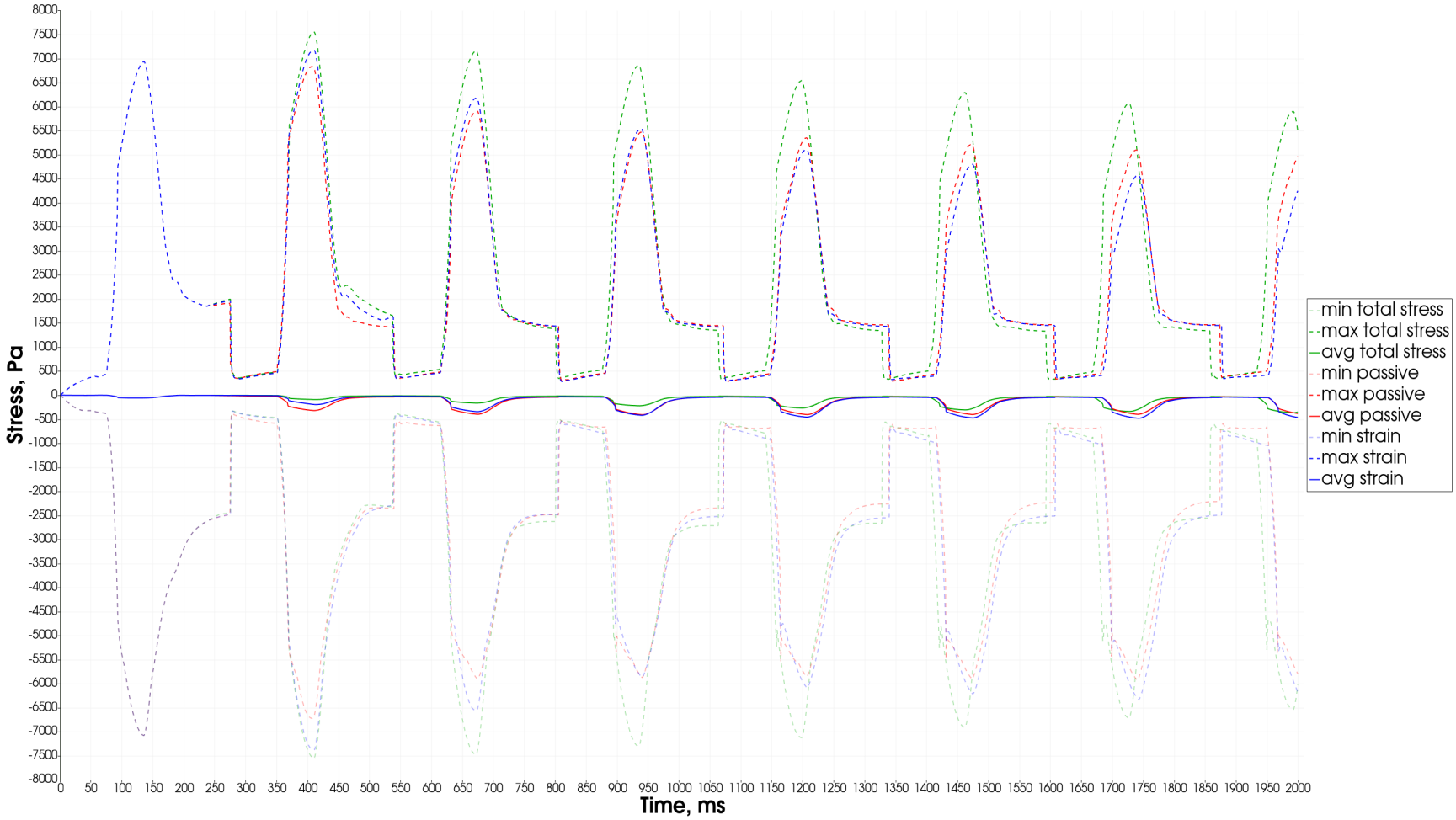

Figure 3.8 Maximum and minimum fiber-sheet total shear stresses over time for the strip simulations. Plot rendered in ParaView 5.7.0.

3.4 Heterogeneous Contractility Simulations

Several preliminary, isometric single-twitch simulations were performed to determine the relationship between the cross-bridge density and the contractile force generated. The results of the study are reported in Figure 3.9. The data reveals a strong linear relationship between cross-bridge density and generated contractile force, given as

$$force = 23.236\, cb - 30.519$$

where *cb* is the cross-bridge density in 1E16 cross bridges per m^2 and *force* is the generated contractile force in kPa. The range of data from this study encompasses ±1.5 SD of cross-bridge density distribution used in the heterogeneous contractile simulations.

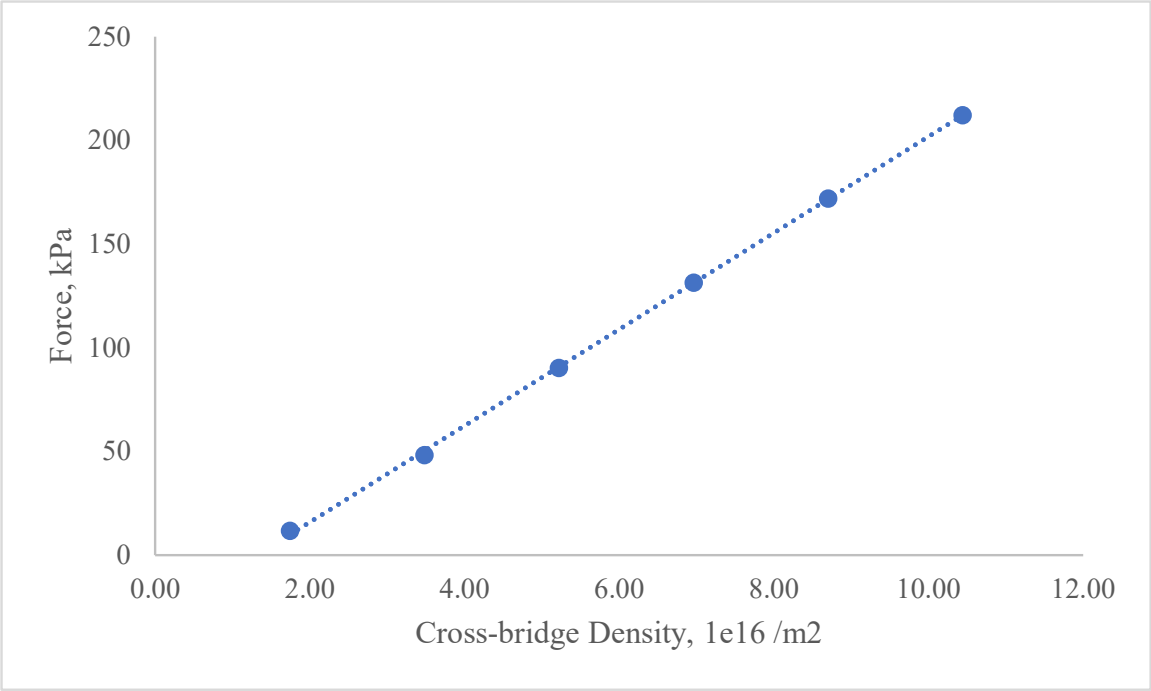

Figure 3.9 Relationship between cross-bridge density and generated force under isometric, single-twitch conditions.

The final fiber orientations for the heterogeneous contractility simulation are shown in Figure 3.10, where total-stress was used as the driver for reorientation. There is marked disorganization among the fibers at the end of the simulation. The angle deviation distribution is shown in Figure 3.11. Statistical measures of the distribution are reported in Table 3.2. Whereas the mode for fiber orientation was within 1.5 degrees of the x-axis in the interstitial fibrosis simulations, the mode for the heterogeneous contraction simulation was within the second bin (1.84 - 3.67 degrees). These measures of distribution indicate that more disorganization was generated in the heterogeneous contractility simulation, compared to the interstitial fibrosis simulations. The maximum and minimum fiber-sheet total shear stress is reported over time in Figure 3.12. The maximum and minimum shear stresses before reorientation were 3242.71 and -4340.22 Pa, respectively. The maximum

shear stress was reduced by 62.71%, and the minimum shear stress was reduced by 67.9%. Note that the maximum and minimum shear stresses were reached simultaneously in the first cycle but occurred at different points in the cycle as reorientation advanced.

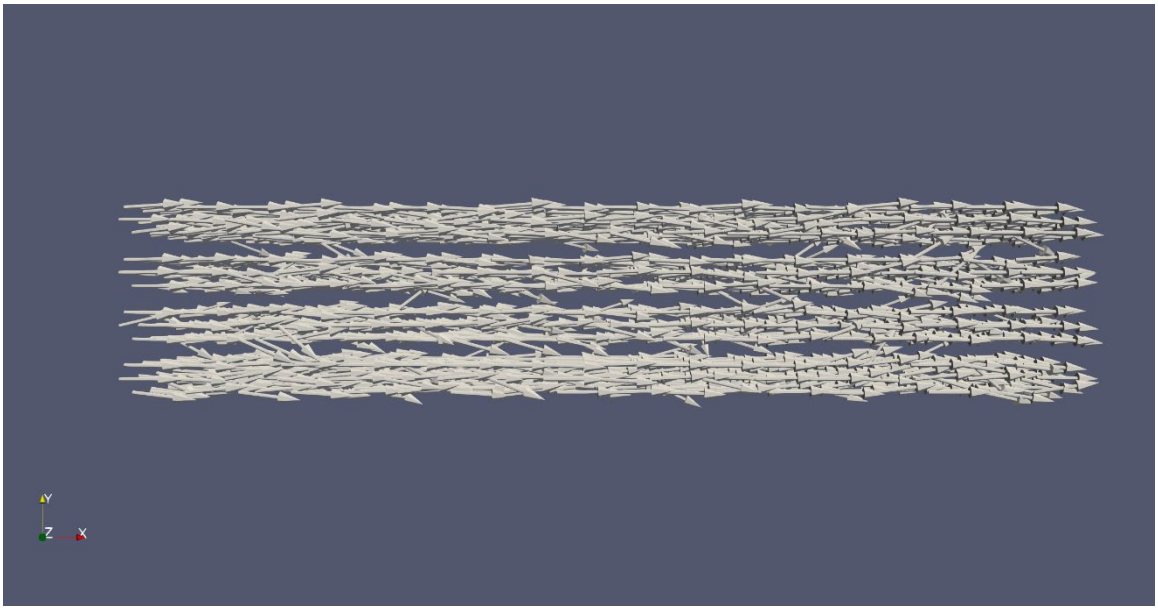

Figure 3.10 Final fiber orientations for total stress-based heterogeneous contractility simulation. Glyph rendered in ParaView 5.7.0.

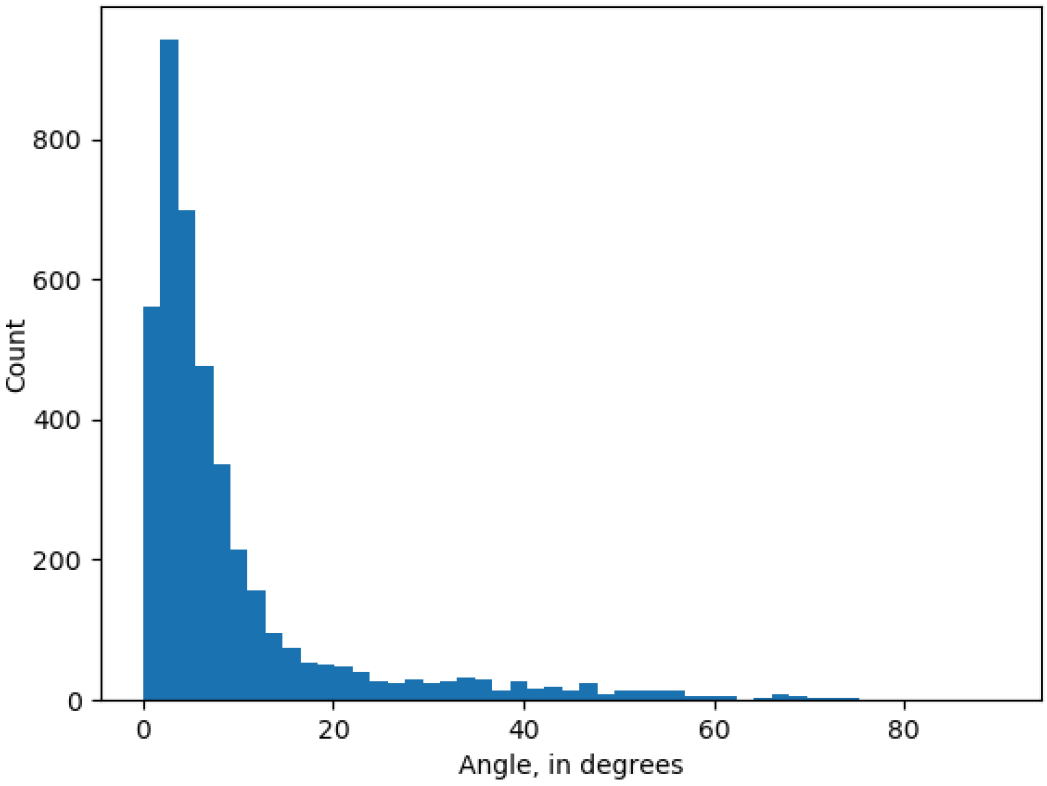

Figure 3.11 Heterogeneous contractility angle distribution at the end of the simulation.

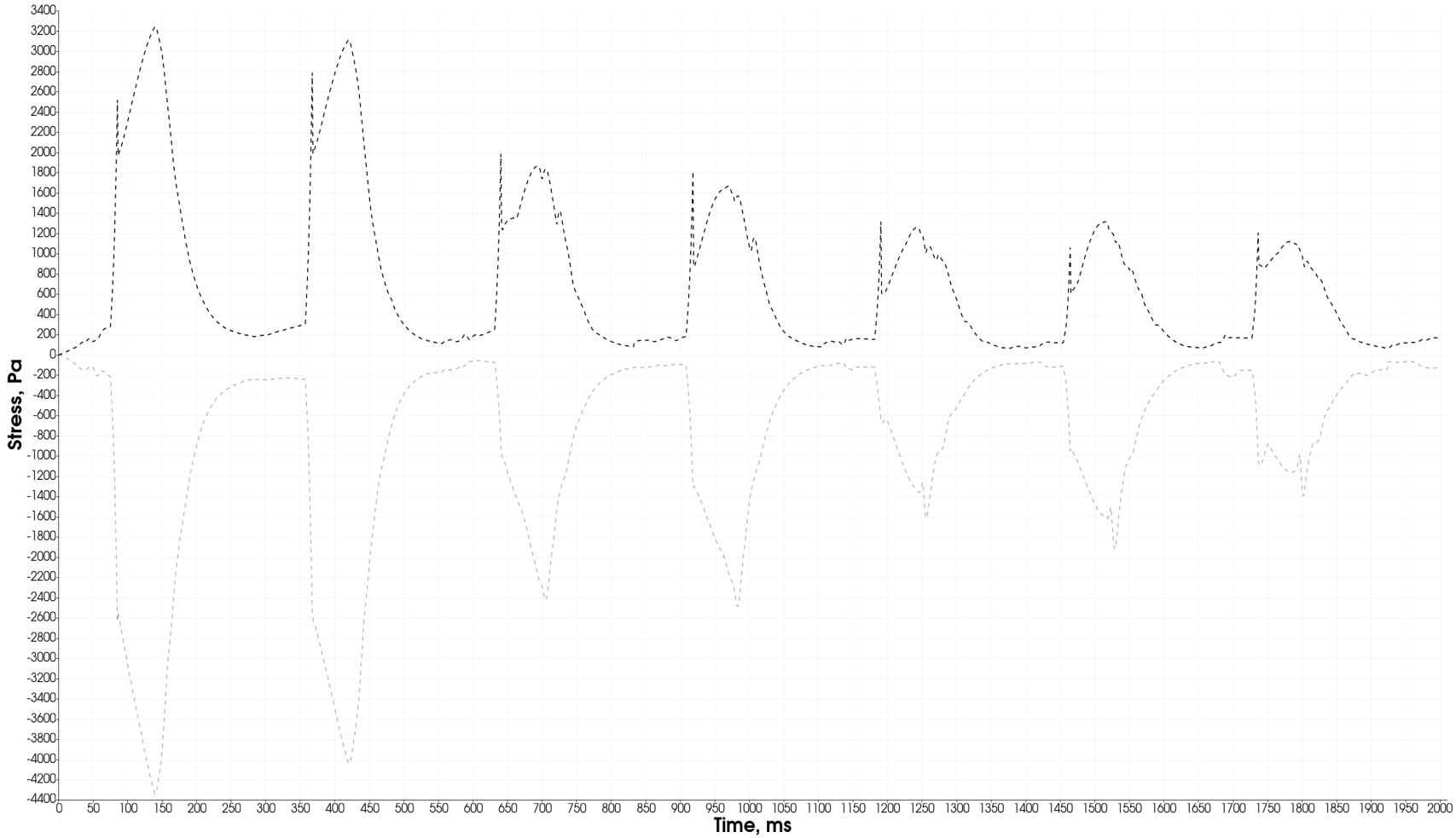

Figure 3.12 Maximum and minimum fiber-sheet shear stresses over time in the heterogeneous contractility simulations. Plot rendered in ParaView 5.7.0.

CHAPTER 4. DISCUSSION

The fiber offset studies in the uniaxial and inclusion simulations suggest that the final solution is dependent on initial fiber orientations as well as boundary conditions. The dependence of the final orientation on initial fiber orientation in the uniaxial simulations is expected, as both the stress- and strain-based reorientation laws adapt towards one of the two corresponding eigenvector solutions. In truth, the uniaxial and simple shear simulations were performed in order to confirm this behavior and thus to serve a foundation for understanding and anticipating behavior in more complex stress states. The influence of initial fiber orientation is more prominent in the inclusion simulations, where the steady-state fiber orientations varied dramatically with initial fiber orientation.

Boundary conditions also have a great impact on the final fiber orientation. In the uniaxial, 225-degree fiber offset case, the choice of boundary conditions can change the final orientation by subtly altering the stress and strain states in the mesh. The loading conditions produces a much greater impact on the stress and strain states. For the fiber offset inclusion simulations, the uniaxial loading conditions produces a relatively homogeneous strain pattern throughout the simulation while the stress patterns vary regionally and evolve as the simulation progresses, resulting in fiber orientation solutions developing in communication with neighboring fibers with different local stress information. In this study, the boundary conditions are simplified in order that the potential for the stress-based reorientation law to produce disarray may be preliminarily evaluated. However, this dependence on boundary conditions also means that the performance of the stress-based reorientation law as shown in this work may not reflect the true adaptation of

cardiomyocytes in vivo. To fully evaluate the merit of the stress-based reorientation law, studies with a more realistic mesh geometry and boundary conditions are required.

Interestingly, the active stress-based adaptation for the interstitial fibrosis case did not result in any reorientation in fiber direction. This is a result of the contractile model in this work. The contractile model used in the work calculates the contraction force per area along the fiber direction and transmits a portion of the force into the sheet and normal directions. The assumption here is that the modeled cardiomyocyte cannot experience shear stresses. Therefore, without any variability in contraction between neighboring elements, no active shear stress is produced, and the fiber direction is always in the direction of maximum traction. However, this is not so in vivo. The branching structure of cardiomyocytes enables the transmission of forces in directions offset from the local basis and is likely responsible for the production of shear stresses due to contraction. A more sophisticated model of the branching structure which allows the transmission of active stress in directions other than fiber, sheet, and normal direction will enable the use of active stress as a sole driver of adaptation.

Washio et al. (2020) achieved physiological and pathological fiber adaptation, driven by active stress, using a contraction model incorporating primary and peripheral fiber directions. The orientations of the peripheral fibers are constant while weights representing the fiber strength are adapted throughout the simulations. However, multiplying the number of contraction calculations performed would produce unreasonable computational loads in our current framework, so perhaps a similar approach can be adopted in which the fiber directions, rather than the fiber strengths, are updated. In any

case, further study towards a more robust representation of myocyte branching structure is required.

The stress- and strain-based reorientation laws successfully induced disorganization in the interstitial fibrosis simulations. The passive stress and strain-based adaptations yielded similar results in terms of directional disorganization, and the final orientations for each simulation qualitatively resemble myocyte disarray in HCM depicted in the literature (Maron et al, 1982; Varnava et al, 2001; Kanzaki et al., 2012). Although the comparatively long tail to the right potentially suggests a higher level of sensitivity to local heterogeneities, the total stress-based adaptation, by contrast, produced the least amount of disarray for the interstitial fibrosis case. However, the performance of the total stress-based adaptation law may not reflect an insufficiency in the stress-based law itself. Rather, the limitation imposed by the calculation of the active stress may result in the constraining of the total stress-based law, if the active stress is indeed a prominent driver of myocyte adaptation, as suggested by works from Washio et al. (2020). Furthermore, validation of these results in comparison with experimental data is necessary to draw conclusions concerning the merit of one reorientation law over another.

It has been suggested that contractile heterogeneity among cardiomyocytes is a major feature of expression for certain familial HCM mutations and that myocyte disarray may develop as a result of this feature (Kraft et al., 2019). To test the potential of heterogeneous contraction to generate myocyte disarray, total stress-based adaptation was allowed to occur in a strip geometry with heterogeneous contractile properties. The resulting final fiber orientations provide support for heterogeneous contractile properties to be a potential trigger for the development of myocyte disarray.

CHAPTER 5. CONCLUSIONS AND FUTURE WORK

Myocyte disarray is one of the major hallmarks of familial hypertrophic cardiomyopathy and can contribute to the impaired global cardiac function observed in HCM patients. However, little work has been done to capture the development and effects of myocyte disarray as a result of fiber adaptation in current models of the heart. In this work, we aimed to develop a continuously adapting, stress-based reorientation law that can reproduce myocyte disarray. The stress-based law demonstrated the ability to produce disorganized fiber orientations which resemble disarrayed myocytes in the cases of heterogeneous passive material and contractile properties. Recommended future works include performing fiber adaptation in a left ventricle model with realistic hemodynamic loading conditions, validating simulation results with experimental data, and developing a more robust representation of the myocyte branching structure.

REFERENCES

Adomian, G. E., & Beazell, J. (1986). Myofibrillar disarray produced in normal hearts by chronic electrical pacing. *American Heart Journal*, *112*(1), 79–83. https://doi.org/10.1016/0002-8703(86)90682-4

Arts, T., Prinzen, F. W., Snoeckx, L. H., Rijcken, J. M., & Reneman, R. S. (1994). Adaptation of cardiac structure by mechanical feedback in the environment of the cell: a model study. *Biophysical Journal*, *66*(4), 953–961. https://doi.org/10.1016/S0006-3495(94)80876-8

Arts, T., Veenstra, P. C., & Reneman, R. S. (1982). Epicardial deformation and left ventricular wall mechanics during ejection in the dog. *American Journal of Physiology - Heart and Circulatory Physiology*, *12*(3). https://doi.org/10.1152/ajpheart.1982.243.3.h379

Arts, Theo, Reneman, R. S., & Veenstra, P. C. (1979). A model of the mechanics of the left ventricle. *Annals of Biomedical Engineering*, *7*, 299–318. https://doi.org/10.1007/BF02364118

Becker, A. E., & Caruso, G. (1982). Myocardial disarray. A critical review. *Heart*, *47*(6), 527–538. https://doi.org/10.1136/hrt.47.6.527

Bovendeerd, P. H. M., Rijcken, J., Campen, D. H. Van, Schoofs, A. J. G., Nicolay, K., & Arts, T. (1999). *Optimization of Left Ventricular Muscle Fiber Orientation*. 285–296. https://doi.org/10.1007/0-306-46939-1_25

Bovendeerd, Peter H M. (2012). Modeling of cardiac growth and remodeling of myofiber orientation. *Journal of Biomechanics*, *45*(5), 872–881. https://doi.org/10.1016/j.jbiomech.2011.11.029

Bulkley, B. H., Weisfeldt, M. L., & Hutchins, G. M. (1977). Asymmetric septal hypertrophy and myocardial fiber disarray. Features of normal, developing, and malformed hearts. *Circulation*, *56*(2), 292–298. https://doi.org/10.1161/01.CIR.56.2.292

Campbell, K. S. (2014). Dynamic coupling of regulated binding sites and cycling myosin heads in striated muscle. *Journal of General Physiology*, *143*(3), 387–399. https://doi.org/10.1085/jgp.201311078

Davies, M. J. (1984). The current status of myocardial disarray in hypertrophic cardiomyopathy. *Heart*, *51*(4), 361–363. https://doi.org/10.1136/hrt.51.4.361

Geerts, L., Bovendeerd, P., Nicolay, K., & Arts, T. (2002). Characterization of the normal cardiac myofiber field in goat measured with MR-diffusion tensor imaging., *283*(1 52-1), 139–145. https://doi.org/10.1152/AJPHEART.00968.2001

Guccione, J. M., Waldman, L. K., & McCulloch, A. D. (1993). Mechanics of actiwe contraction in cardiac muscle: Part II—cylindrical models of the systolic left ventricle. *Journal of Biomechanical Engineering*, *115*(1), 82–90.

https://doi.org/10.1115/1.2895474

Kanzaki, Y., Yamauchi, Y., Okabe, M., Terasaki, F., & Ishizaka, N. (2012). Three-dimensional architecture of cardiomyocytes and connective tissues in hypertrophic cardiomyopathy: A scanning electron microscopic observation. *Circulation*, *125*(6), 738–739. https://doi.org/10.1161/CIRCULATIONAHA.111.054668

Kraft, T., & Montag, J. (2019). Altered force generation and cell-to-cell contractile imbalance in hypertrophic cardiomyopathy. *European Journal of Physiology*. https://doi.org/10.1007/s00424-019-02260-9

Kraft, T., Witjas-Paalberends, E. R., Boontje, N. M., Tripathi, S., Brandis, A., Montag, J., Hodgkinson, J. L., Francino, A., Navarro-Lopez, F., Brenner, B., Stienen, G. J. M., & Van der Velden, J. (2013). Familial hypertrophic cardiomyopathy: Functional effects of myosin mutation R723G in cardiomyocytes. *Journal of Molecular and Cellular Cardiology*, *57*(1), 13–22. https://doi.org/10.1016/j.yjmcc.2013.01.001

Kroon, W., Delhaas, T., Bovendeerd, P., & Arts, T. (2009). Computational analysis of the myocardial structure: Adaptation of cardiac myofiber orientations through deformation. *Medical Image Analysis*, *13*(2), 346–353. https://doi.org/10.1016/j.media.2008.06.015

Kuribayashi, T., & Roberts, W. C. (1992). Myocardial disarray at junction of ventricular septum and left and right ventricular free walls in hypertrophic cardiomyopathy. *The American Journal of Cardiology*, *70*(15), 1333–1340. https://doi.org/10.1016/0002-9149(92)90771-P

Mann, C. K., Lee, L. C., Campbell, K. S., & Wenk, J. F. (2020). Force-dependent recruitment from myosin OFF-state increases end-systolic pressure–volume relationship in left ventricle. *Biomechanics and Modeling in Mechanobiology*, *19*(6), 2683–2692. https://doi.org/10.1007/S10237-020-01331-6

Maron, B. J., Anan, T. J., & Roberts, W. C. (1981). Quantitative analysis of the distribution of cardiac muscle cell disorganization in the left ventricular wall of patients with hypertonic cardiomyopathy. *Circulation*, *63*(4), 882–894. https://doi.org/10.1161/01.CIR.63.4.882

Maron, Barry J. (2002). Hypertrophic cardiomyopathy: A systematic review. *Journal of the American Medical Association*, *287*(10), 1308–1320. https://doi.org/10.1001/jama.287.10.1308

Rijcken, J., Bovendeerd, P. H. M., Schoofs, A. J. G., Van Campent, D. H., & Arts, T. (1997). Optimization of cardiac fiber orientation for homogeneous fiber strain at beginning of ejection. *Journal of Biomechanics*, *30*(10), 1041–1049. https://doi.org/10.1016/S0021-9290(97)00064-X

Rohmer, D., Sitek, A., & Gullberg, G. T. (2007). Reconstruction and Visualization of Fiber and Laminar Structure in the Normal Human Heart from Ex Vivo Diffusion Tensor Magnetic Resonance Imaging (DTMRI) Data. *Investigative Radiology*, *42*(11), 777-789. www.ccbm.jhu.edu/research/DTMRIDS.php

Sedmera, D. (2005). Form follows function: Developmental and physiological view on ventricular myocardial architecture. *European Journal of Cardio-thoracic Surgery*, *28*(4), 526–528. https://doi.org/10.1016/j.ejcts.2005.07.001

Van Der Bel-Kahn, J. (1977). Muscle fiber disarray in common heart diseases. *The American Journal of Cardiology*, *40*(3), 355–364. https://doi.org/10.1016/0002-9149(77)90157-6

Varnava, A M. (2000). Hypertrophic cardiomyopathy: the interrelation of disarray, fibrosis, and small vessel disease. *Heart*, *84*(5), 476–482. https://doi.org/10.1136/heart.84.5.476

Varnava, Amanda M., Elliott, P. M., Mahon, N., Davies, M. J., & McKenna, W. J. (2001). Relation between myocyte disarray and outcome in hypertrophic cardiomyopathy. *American Journal of Cardiology*, *88*(3), 275–279. https://doi.org/10.1016/S0002-9149(01)01640-X

Washio, T., Sugiura, S., Okada, J., & Hisada, T. (2020). Using Systolic Local Mechanical Load to Predict Fiber Orientation in Ventricles. *Frontiers in Physiology*, *11*. https://doi.org/10.3389/fphys.2020.00467

Washio, T., Yoneda, K., Okada, J.-I., Kariya, T., Sugiura, S., & Hisada, T. (2016). Ventricular fiber optimization utilizing the branching structure. *International Journal of Numerical Methods in Biomedical Engineering*. https://doi.org/10.1002/cnm.2753

Xi, C., Kassab, G. S., & Lee, L. C. (2019). Microstructure-based finite element model of left ventricle passive inflation. *Acta Biomaterialia* 90, 241-253. https://doi.org/10.1016/j.actbio.2019.04.016

VITA

EDUCATION

- University of Kentucky, Lexington, KY
    - Bachelor of Science in Mechanical Engineering, May 2019

PROFESSIONAL POSITIONS

- Graduate Research Assistant, 2019-
- Undergraduate Research Assistant, 2016-2017

HONORS AND AWARDS

- NHLBI Research Supplement (PA-18-586), 2019
- Presidential Scholarship, University of Kentucky, 2014-2018
- Scholarship, National Achievement Scholarship Program, 2016

PUBLICATIONS

- Sharifi H, Mann CK, **Rockward AL**, Mohammad M, Mojumder J, Lik-Chuan L, Campbell KS, Wenk JF. "Multiscale modeling of cardiac growth and remodeling." *Biophysics Reviews* (2021). Paper submitted and under review.